Dalton Transactions

Accepted Manuscript

ROYAL SOCIETY OF CHEMISTRY

www.rsc.org/dalton

Synthesis and Characterization of Substituted Schiff-base Ligands and Their d^{10} Metal Complexes: Structure-induced Luminescence Tuning Behaviors and Applications in Co-sensitized Solar Cells

Yu-Wei Dong,[a] Rui-Qing Fan,*[a] Ping Wang,[a] Li-Guo Wei,[a] Xin-Ming Wang,[a] Hui-Jie Zhang,[a] Song Gao,[a] Yu-Lin Yang*[a] and Yu-Lei Wang[b]

[a]*Department of Chemistry, Harbin Institute of Technology, Harbin 150001, P. R. of China*

[b]*National Key Laboratory of Science and Technology on Tunable Laser, Harbin Institute of Technology, Harbin 150080, P. R. of China*

To whom the proofs and correspondence should be sent.

Associate Professor Rui-Qing Fan and Yu-Lin Yang
Department of Chemistry
Harbin Institute of Technology Harbin 150001, P. R. China
Fax: +86-451-86413710
E-mail: fanruiqing@hit.edu.cn and ylyang@hit.edu.cn

Nine IIB group complexes, [Zn$\mathbf{L_1}$$Cl_2$] (**Zn1**), [Cd$\mathbf{L_1}$$Cl_2$]$_2$ (**Cd1**), [Hg$\mathbf{L_1}$$Cl_2$] (**Hg1**), [Zn$\mathbf{L_2}$$Cl_2$] (**Zn2**), [Cd$\mathbf{L_2}$$Cl_2$] (**Cd2**), [Hg$\mathbf{L_2}$$Cl_2$] (**Hg2**), [Zn$\mathbf{L_3}$$Cl_2$] (**Zn3**), [Cd$\mathbf{L_3}$$Cl_2$] (**Cd3**) and [Hg$\mathbf{L_3}$$Cl_2$] (**Hg3**) have been synthesized by the corresponding ortho-(6-methoxy-pyridyl)(CH=NAr) (Ar = 2,6–*i*$Pr_2C_6H_3$, $\mathbf{L_1}$; 4–MeC_6H_4, $\mathbf{L_2}$; 2–$OMeC_6H_4$, $\mathbf{L_3}$) schiff-base and structurally characterized by elemental analysis, FT-IR, ^{1}H NMR and X-ray single-crystal analysis. Crystallographic studies reveal that center metal of complexes adopt distorted tetrahedron geometry (except for **Cd1** and **Cd3**, which they display square pyramid geometry) and C–H···Cl hydrogen bonds and π···π stacking interactions contribute to three-dimensional supramolecular structures. The series of complexes exhibit tunable luminescence from blue, green to light yellow by varying the temperature (298 K and 77 K) in the solution and in the solid state. Moreover, the quantum yields range from 0.027 to 0.422, which decrease according to the order of the periodic table (Zn > Cd > Hg). These results indicate that the center atom of the complexes lead to the geometry differences and then tune the luminescence properties. Since **Zn1**–**Zn3** exhibited higher molar extinction coefficients and proper absorption region, they were employed as co-sensitizer in ruthenium dye N719 sensitized photoanodes to assemble with counter electrodes and electrolyte to prepare ZnX/N719 (ZnX = **Zn1**, **Zn2** and **Zn3**) co-sensitized dye sensitized solar cells (DSSCs) devices from the view of light-electricity efficiency enhancement. The prepared co-adsorbent could overcome the deficiency of N719 absorption in the low wavelength region of visible spectrum, offset competitive visible light absorption of I_3^-. Application of these prepared complexes in N719 sensitized solar cell do enhanced its performance by 10%–36%, which indicates a potential application of such kind of complexes in DSSCs.

1. Introduction

Recently, the design and synthesis of organic–inorganic hybrid complexes based on strong coordinate bonds and multiple weak non-covalent forces have become a research field of rapid expansion in coordination chemistry and crystal engineering. It not only possesses fascinating structural features but also shows interesting properties as new functional materials, which can be used in the areas of luminescence, sensors, separation, adsorption, catalysis and biological chemistry, etc.[1–4] Moreover, researchers begin to focus on the potential applications of organometallic complex with optical properties in co-sensitized dye sensitized solar cells (DSSCs) in recent years.[5, 6]

Zn(II), Cd(II) and Hg(II) ions often adopt different coordination modes, such as four-, five- or six-coordination modes when they react with organic ligands with N, O donors.[7] The design and synthesis of new organic ligands is a key approach for construction of metal–organic complexes with desired structures. Schiff-base still play an important role in metal coordination chemistry even after almost a century since their discovery.[8] They are considered “privileged ligands” and are the most widely used due to their multitudinous synthesis, remarkable versatility and good solubility in common solvents. A large number of schiff-base have been synthesized and extensively studied because they have some characteristic properties such as manifestations of novel structures, thermal stability, relevant biological properties, high synthesis flexibility and medicinal utility.[9] The possibility of structural changes and the existence of different supramolecular structures after coordination are the key phenomena responsible for the photochromic behavior of the complex based on aromatic schiff-base with hydrogen bonds.[10] Relatively complex photobehaviour of these complexes related to their rotational flexibility has to be well understood.[11] The introduction of different small anions can also have a significant effect on the structural construction of complexes and their properties. In coordination chemistry, halogen ions have been widely used as anions for the construction of the metal coordination complexes because they can adjust the topologies of complexes through

different coordinate bonds or non-covalent interactions.[12]

To gain insight into the influence of schiff-base ligands with different functional groups in constructing Zn(II), Cd(II) and Hg(II) complexes, we studied the synthesis, stability, and photoelectric properties of complexes using the following three new synthesis schiff-base, namely, ortho-(6-methoxy-pyridyl)(CH=NAr) (Ar = 2,6–*i*Pr$_2$C$_6$H$_3$, **L$_1$**; 4–MeC$_6$H$_4$, **L$_2$**; 2–OMeC$_6$H$_4$, **L$_3$**). By self-assembly, a series of novel Zn(II), Cd(II) and Hg(II) complexes were synthesized, [Zn**L$_1$**Cl$_2$] (**Zn1**), [Cd**L$_1$**Cl$_2$]$_2$ (**Cd1**), [Hg**L$_1$**Cl$_2$] (**Hg1**), [Zn**L$_2$**Cl$_2$] (**Zn2**), [Cd**L$_2$**Cl$_2$] (**Cd2**), [Hg**L$_2$**Cl$_2$] (**Hg2**), [Zn**L$_3$**Cl$_2$] (**Zn3**), [Cd**L$_3$**Cl$_2$] (**Cd3**) and [Hg**L$_3$**Cl$_2$] (**Hg3**). The rational design of schiff-base with functional group in different position not only influences structural varieties but also considerably determines the luminescent properties.[13] Generally, the scale of π-conjugated system and the electronic effect of substituents on the ligand are effective factors for controlling emission color as well as their photoluminescence efficiencies.[14] In consideration of the absorb light in the low wavelength region of the visible spectrum,[15] we used **Zn1**–**Zn3** which have suitable absorption and energy levels to prepare ZnX/N719 co-sensitized dye sensitized solar cells (DSSCs) devices from the view of light-electricity efficiency enhancement. The application of these prepared complexes in N719 sensitized solar cell enhanced the performance by 10%–36%, which indicates a potential application in DSSCs.

2. Experimental Section

General information. All reagents were analytical grade from commercial sources and were used directly without any further purification. Anilne derivants (2,6-diisopropylaniline, 4-methylaniline and 2-methoxyaniline) and 6-methoxy-2-pyridinecarboxaldehyde were purchased from Aldrich Co., Ltd and Rui Yi Sci. & Tec. Co. Ltd. (Shanghai, China), respectively. Metal salts were purchased from Ji Nan Henghua Sci. & Tec. Co. Ltd. (Shandong, China). Solvents for reaction and photophysical studies were dried and freshly distilled under dry nitrogen gas before using. ^{1}H NMR (400 MHz) spectra were recorded on a Bruker Avance-400 spectrometer using Si(CH$_3$)$_4$ as an internal standard at room temperature. Elemental

analysis for C, H, and N were performed on a Perkin-Elmer 2400 automatic analyzer. Fourier transform (FT)-IR spectra were measured on a Perkin-Elmer Spectrum 100 FT-IR Spectrometer with samples prepared as KBr discs. UV-vis spectra were recorded on a Perkin-Elmer Lambda 35 spectrometer. The cyclic voltammetry (CV) were measured with a CHI660d electrochemical workstation (Shanghai, China) using a three-elctrode cell with a Pt working electrode, a Pt wire auxiliary electrode, and a saturated calomel reference electrode in saturated KCl solution. The supporting electrolyte was 0.1 M teterabutylammonium hexafluorophosphate (TBAPF6, Fluka, electrochemical grade) in ethanol as the solvent. The solid-state and solution photoluminescence analyses were carried out on an Edinburgh FLS920 fluorescence spectrometer in the range of 200–800 nm. The visible detector as well as the lifetime setup is red-sensitive photomultiplier (type r928). Lifetime studies were performed using photon-counting system with a microsecond pulse lamp as the excitation source. The emission decays were analyzed by the sum of exponential functions. The decay curve is well fitted into a double exponential function: $I = I_0 + A_1 \exp(-t/\tau_1) + A_2 \exp(-t/\tau_2)$, where I and I_0 are the luminescent intensities at time $t = t$ and $t = 0$, respectively, whereas τ_1 and τ_2 are defined as the luminescent lifetimes. The average lifetime was calculated according to the following equation (1): $\frac{\tau_1^2 A_1\% + \tau_2^2 A_2\%}{\tau_1 A_1\% + \tau_2 A_2\%}$ (1). The luminescence quantum yields of complexes were measured in CH_3CN at room temperature and cited relative to a reference solution of quinine sulfate ($\Phi = 0.546$ in 0.5 mol dm^{-3} H_2SO_4) as a standard, and they were calculated according to the well-known equation (2):[10] $\frac{\varphi_{overall}}{\varphi_{ref}} = \left(\frac{n}{n_{ref}}\right)^2 \frac{A_{ref}}{A} \frac{I}{I_{ref}}$ (2). In equation (2), n, A, and I denote the refractive index of solvent, the area of the emission spectrum, and the absorbance at the excitation wavelength, respectively, and φ_{ref} represents the quantum yield of the standard quinine sulfate solution. The subscript *ref* denotes the reference, and the absence of a subscript implies an unknown sample. For the determination of the quantum yield, the excitation wavelength was chosen so that $A < 0.05$.

X-ray structure determinations of complexes. Single crystals of nine complexes suitable for X-ray structural analysis were obtained from CH_3OH or CH_3OH/CH_2Cl_2. Diffraction data were collected on a Rigaku R-AXIS RAPID IP diffractometer equipped with graphite-monochromated Mo-Kα radiation (λ = 0.71073 Å), operating at 293 ± 2 K. Details of the crystal data, data collection and structure refinements are summarized in Table 1. The structures were solved by direct methods and refined by full-matrix least-squares based on F^2 using the SHELXTL 5.1 software package (Sheldrick G M. SHELXTL NT Crystal Structure Analysis Package [CP]. version 5.10; Bruker AXS, Analytical X-ray System: Madison, WI, 1999). The hydrogen atoms residing on the carbon atoms were located geometrically. All non-hydrogen atoms were refined anisotropically.

Assembly and measurement of DSSCs. Dye-sensitized solar cells were fabricated using the following procedure. The TiO_2 paste was cast onto the FTO substrate by the screen-printing method, followed by drying at 100 ºC for 5 min and this process was repeated for six times, then followed by sinterings at 500 ºC for 15 min in air to obtain a transparent TiO_2 photoelectrode with the thickness of *ca*. 10 μm. The co-sensitized electrodes were prepared by immersing the obtained mesoporous TiO_2 photoelectrode into 0.3 mM **Zn1**, **Zn2** or **Zn3** solution in absolute ethanol for 2 h and washed with ethanol and dried with blower, then further immersing the electrodes in 0.3 mM N719 solution in absolute ethanol for 12 h, and then washed with ethanol and dried with blower again. The single N719 sensitized electrodes were prepared by only immersing TiO_2 photoelectrode into 0.3 mM N719 solution in absolute ethanol for 14 h. The electrolyte used in this work was 0.5 M LiI + 0.05 M I_2 + 0.1 M tert-butyl pyridine in a 1:1 (volume ratio) of acetonitrile-propylene carbonate. The platinum counter electrode was prepared by depositing H_2PtCl_6 paste onto the FTO glass substrates and then sintered at 450 ºC for 30 min. The cells were assembled by sandwiching the electrolyte between the dye sensitized photoanode and the counter electrode and assembly was held together using mini-binder clips.

Photocurrent-photovoltage (*I-V*) curves were recorded by Keithley model 2400 digital source meter using a mask with an aperture area of 0.16 cm^2. The irradiance of

AM 1.5 global sunlight from a filtered 500 W xenon lamp light source was set at 100 mW cm^{-2} and was calibrated by a standard silicon solar cell (NO. NIMMS1123, calibrated by National Institute of Metrology, P. R. China). Based on *I-V* curve, the fill factor (*FF*) is defined as: $FF = (J_{max} \times V_{max})/(J_{sc} \times V_{oc})$ where J_{max} and V_{max} are the photocurrent density and photovoltage for maximum power output; J_{sc} and V_{oc} are the short-circuit photocurrent density and open-circuit photovoltage, respectively. The overall energy conversion efficiency η is defined as: $\eta = (FF \times J_{sc} \times V_{oc})/P_{in}$ where P_{in} is the power of the incident light. EIS were recorded by CHI660D Electrochemical Analyzer (Chenhua, China), and the measurements were taken over a frequency range of 0.1-100 kHz under standard global AM1.5 solar irradiation. Dark current were also recorded by CHI660D Electrochemical Analyzer.

Synthesis of the ligands and complexes. (*E*)-2,6-diisopropyl-*N*-((6-methoxypyridin-2-yl)methylene)aniline (L_1). A mixture of 2,6-diisopropylaniline (3.15 mL, 16.70 mmol) and 6-methoxy-2-pyridinecarboxaldehyde (2.0 mL, 16.63 mmol) was refluxed in anhydrous methanol (30 mL) in the presence of a catalytic amount of formic acid for 12 h. After the reaction was over, the resulting solution was concentrated under reduced pressure (oil pump) to obtain the pale yellow solid. The crude product was recrystallized from *n*-hexane to give the pale yellow solid. Yield: 4.23 g (85 %). Anal. Calcd for **L_1** [$C_{19}H_{24}N_2O$ (296.41)]: C, 76.99; H, 8.16; N, 9.45 %. Found: C, 76.78; H, 8.22; N, 9.42 %. ^{1}H NMR (400 MHz, $CDCl_3$, 298K): δ 8.18 (s, 1H, C*H*=N), 7.85 (d, 1H, Py-H_5), 7.72 (t, 1H, Py-H_4), 7.26 (s, 1H, Py-H_3), 6.85-7.16 (m, 3H, Ph-*H*), 3.99 (s, 3H, OCH_3), 2.97 (m, 2H, C*H*), 1.28 (d, 12H, CH_3) ppm. FT-IR (KBr): ν 3436 (m), 3065 (w), 2962 (m), 2870 (m), 1647 (s), 1589 (s), 1467 (vs), 1413 (m), 1327 (m), 1268 (m), 1180 (w), 1143 (m), 1072 (w), 934 (w), 858 (m), 812 (w), 747 (s), 631 (w), 530 (w), 451(w) cm^{-1}.

(*E*)-4-methyl-*N*-((6-methoxypyridin-2-yl)methylene)aniline (L_2). The procedure is similar to that of **L_1**, except that 4-methylaniline (1.78 g, 16.61 mmol) was used instead of 2,6-diisopropylaniline. **L_2** was obtained as a yellow bluk solid. Yield: 2.91 g (77 %). Anal. Calcd for **L_2** [$C_{14}H_{14}N_2O$ (226.27)]: C, 74.31; H, 6.24; N, 12.38 %. Found: C, 74.16; H, 6.38; N, 12.20 %. ^{1}H NMR (400 MHz, $CDCl_3$, 298K): δ 8.50 (s, 1H, C*H*=N), 7.77 (d, 1H, Py-H_5), 7.67 (t, 1H, Py-H_4), 7.21 (s, 4H, Ph-*H*), 6.81 (d, 1H,

Py-H_3), 4.00 (s, 3H, OCH_3), 2.38 (s, 3H, CH_3) ppm. FT-IR (KBr): *v* 3433 (w), 3023 (w), 2978 (m), 2858 (w), 1628 (m), 1587 (vs), 1471 (vs), 1432 (s), 1417 (m), 1324 (s), 1269 (vs), 1151 (m), 1074 (m), 1036 (vs), 964 (m), 869 (m), 810 (vs), 733 (m), 632 (m), 527 (m), 483(w) cm^{-1}.

(*E*)-2-methoxy-*N*-((6-methoxypyridin-2-yl)methylene)aniline (L_3). The procedure is similar to that of L_1, except that 2-methoxyaniline (1.90 g, 16.94 mmol) was used instead of 2,6-diisopropylaniline. L_3 was obtained as brown yellow oil. Yield: 4.03 g (89 %). Anal. Calcd for L_3 [$C_{14}H_{14}N_2O_2$ (242.27)]: C, 69.41; H, 5.82; N, 11.56 %. Found: C, 69.17; H, 5.99; N, 11.38 %. ^{1}H NMR (400 MHz, $CDCl_3$, 298K): δ 8.50 (s, 1H, C*H*=N), 7.85 (d, 1H, Py-H_5), 7.73 (t, 1H, Py-H_4), 7.56 (d, 1H, Py-H_3), 6.71-7.09 (m, 4H, Ph-*H*), 4.03 (s, 3H, Py-OCH_3), 3.99 (s, 3H, Ph-CH_3) ppm. FT-IR (KBr): *v* 3410 (m), 3064 (w), 2950 (m), 2835 (w), 2591 (w), 2050 (w), 1719 (m), 1632 (m), 1602 (m), 1516 (m), 1337 (m), 1222 (m), 1178 (m), 1146 (m), 1117 (m), 1073 (m), 1027 (m), 987 (m), 929 (w), 867 (m), 805 (m), 742 (m), 644 (w), 585 (w), 525 (w), 462 (w), 409 (w) cm^{-1}.

[ZnL_1Cl_2] (Zn1). L_1 (59.2 mg, 0.2 mmol) and $ZnCl_2$ (27.3 mg, 0.2 mmol) were refluxed in 25 mL of anhydrous methanol for 9 h. The mixture was then cooled to the room temperature and filtered. The filtrate was allowed to stand at room temperature in air. Yellow bulk crystals **Zn1** were obtained by slow evaporation after 4 days. Yield: 38.9 mg (45 %). Anal. Calcd for **Zn1** [$C_{19}H_{24}Cl_2N_2OZn$ (432.67)]: C, 52.74; H, 5.59; N, 6.47 %. Found: C, 52.50; H, 5.72; N, 6.38 %. ^{1}H NMR (400 MHz, $CDCl_3$, 298K): δ 8.23 (s, 1H, C*H*=N), 8.16 (d, 1H, Py-H_5), 7.73 (t, 1H, Py-H_4), 7.48 (d, 1H, Py-H_3), 6.81-7.33 (m, 3H, Ph-*H*), 4.04 (s, 3H, OCH_3), 3.13 (m, 2H, C*H*), 1.08 (d, 12H, CH_3) ppm. FT-IR (KBr): *v* 3081 (w), 2964 (s), 2867 (m), 1635 (m), 1600 (s), 1575 (s), 1479 (vs), 1428 (m), 1368 (s), 1293 (s), 1217 (w), 1177 (m), 1095 (m), 1062 (w), 1044 (w), 1014 (s), 952 (s), 866 (w), 802 (s), 771 (m), 740 (w), 699 (w), 595 (w), 536 (w), 506 (w), 441 (w) cm^{-1}.

[$CdL_1Cl_2]_2$ (Cd1). L_1 (29.6 mg, 0.1 mmol) and $CdCl_2$ (22.8 mg, 0.1 mmol) were refluxed in 25 mL of anhydrous methanol for 6 h. The mixture was then cooled to the room temperature and filtered. The filtrate was allowed to stand at room temperature in air. Colorless bulk crystals **Cd1** were obtained by slow evaporation after 22 days. Yield: 29.7 mg (62 %). Anal. Calcd for **Cd1** [$[C_{19}H_{24}Cl_2N_2OCd]_2$ (959.42)]: C, 47.57; H, 5.04; N, 5.84 %. Found: C, 47.82; H, 4.86; N, 5.95 %. ^{1}H NMR (400 MHz, $CDCl_3$, 298K): δ 8.18 (s, 1H, C*H*=N), 7.84 (d, 1H, Py-H_5), 7.72 (t, 1H, Py-H_4), 7.15 (s, 1H,

Py-H_3), 6.97-7.05 (m, 3H, Ph-*H*), 4.03 (s, 3H, OCH_3), 2.95 (m, 2H, C*H*), 1.18 (d, 12H, CH_3) ppm. FT-IR (KBr): *v* 3452 (m), 3073 (w), 2961 (s), 2866 (w), 1636 (m), 1593 (s), 1576 (m), 1478 (s), 1432 (m), 1370 (m), 1297 (m), 1220 (w), 1174 (m), 1100 (m), 1058 (w), 1043 (w), 1008 (s), 960 (s), 859 (w), 805 (s), 777 (s), 740 (w), 679 (w), 587 (w), 534 (w), 507 (w), 424(w) cm^{-1}.

[HgL_1Cl_2] (Hg1). The procedure is similar to that of **Zn1**, except that $HgCl_2$ (54.3 mg, 0.2 mmol) was used instead of $ZnCl_2$. Yellow bulk crystals **Hg1** were obtained by slow evaporation after 29 days. Yield: 60.2 mg (53 %). Anal. Calcd for **Hg1** [$C_{19}H_{24}Cl_2N_2OHg$ (567.89)]: C, 40.18; H, 4.26; N, 4.93 %. Found: C, 40.53; H, 4.38; N, 4.77 %. ^{1}H NMR (400 MHz, $CDCl_3$, 298K): δ 8.39 (s, 1H, C*H*=N), 8.02 (dd, 1H, Py-H_5), 7.42 (d, 1H, Py-H_4), 7.22 (d, 1H, Py-H_3), 6.97-7.20 (m, 3H, Ph-*H*), 4.16 (s, 3H, OCH_3), 3.09 (m, 2H, C*H*), 1.18 (d, 12H, CH_3) ppm. FT-IR (KBr): *v* 3446 (m), 3065 (w), 2962 (s), 2870 (w), 1647 (s), 1597 (s), 1571 (m), 1467 (vs), 1430 (w), 1413 (m), 1383 (w), 1361 (w), 1327 (s), 1268 (s), 1231 (w), 1180 (w), 1143 (m), 1100 (w), 1072 (w), 1031 (s), 987 (w), 934 (w), 858 (m), 812 (m), 777 (w), 747 (s), 530 (w), 450 (w) cm^{-1}.

[ZnL_2Cl_2] (Zn2). To a 5 mL methanol solution of $ZnCl_2$ (13.3 mg, 0.1 mmol) was slowly added a 25 mL dichloromethane solution of $\mathbf{L_2}$ (22.6 mg, 0.1 mmol) under stirring. The mixture was stirred and heated under reflux for 6 h. The mixture was then cooled to the room temperature and filtered. The filtrate was allowed to stand at room temperature in air. Colorless bulk crystals **Zn2** were obtained by slow evaporation for 3 days. Yield: 24.3 mg (67 %). Anal. Calcd for **Zn2** [$C_{14}H_{14}Cl_2N_2OZn$ (362.56)]: C, 46.37; H, 3.89; N, 7.73 %. Found: C, 46.78; H, 3.97; N, 7.50 %. ^{1}H NMR (400 MHz, $CDCl_3$, 298K): δ 8.60 (s, 1H, C*H*=N), 7.69 (d, 1H, Py-H_5), 7.52 (t, 1H, Py-H_4), 7.30 (m, 4H, Ph-*H*), 7.00 (s, 1H, Py-H_3), 4.27 (s, 3H, OCH_3), 2.42 (s, 3H, CH_3) ppm. FT-IR (KBr): *v* 3440 (w), 3037 (w), 2946 (w), 2883 (w), 1625 (m), 1601 (m), 1569 (s), 1514 (m), 1480 (vs), 1427 (m), 1378 (m), 1299 (s), 1241 (m), 1175 (m), 1100 (s), 1016 (s), 959 (s), 834 (s), 801 (s), 735 (m), 649 (m), 587 (w), 523 (m), 480 (w) cm^{-1}.

[CdL_2Cl_2] (Cd2). The procedure is similar to that of **Cd1**, except that $\mathbf{L_2}$ (22.6 mg, 0.1 mmol) was used instead of $\mathbf{L_1}$. Yellow bulk crystals **Cd2** were obtained by slow evaporation after 22 days. Yield: 22.5 mg (55 %). Anal. Calcd for **Cd2** [$C_{14}H_{14}Cl_2N_2OCd$ (409.58)]: C, 41.05; H, 3.45; N, 6.84 %. Found: C, 41.46; H, 3.29; N, 6.75 %. ^{1}H NMR (400 MHz, $CDCl_3$, 298K): δ 8.55 (s, 1H, C*H*=N), 7.73 (t, 1H,

Py-H_5), 7.56 (d, 1H, Py-H_4), 7.23 (m, 4H, Ph-*H*), 6.99 (d, 1H, Py-H_3), 4.03 (s, 3H, OCH_3), 2.02 (s, 3H, CH_3) ppm. FT-IR (KBr): *v* 3450 (m), 3033 (w), 2941 (w), 2875 (w), 1624 (w), 1601 (m), 1567 (s), 1509 (w), 1477 (vs), 1426 (m), 1374 (m), 1312 (s), 1298 (m), 1239 (w), 1175 (m), 1101 (s), 1008 (s), 961 (s), 833 (m), 818 (s), 801 (s), 734 (w), 648 (w), 582 (w), 520 (m), 471 (w) cm^{-1}.

[HgL_2Cl_2] (Hg2). The procedure is similar to that of **Zn2**, except that $HgCl_2$ (27.2 mg, 0.1 mmol) was used instead of $ZnCl_2$. Yellow bulk crystals **Hg2** were obtained by slow evaporation after 3 days. Yield: 29.9 mg (60 %). Anal. Calcd for **Hg2** [$C_{14}H_{14}Cl_2N_2OHg$ (497.76)]: C, 33.78; H, 2.83; N, 5.63 %. Found: C, 33.54; H, 2.97; N, 5.51 %. ^{1}H NMR (400 MHz, $CDCl_3$, 298K): δ 8.70 (s, 1H, C*H*=N), 8.00 (t, 1H, Py-H_5), 7.73 (t, 1H, Py-H_4), 7.56 (d, 1H, Py-H_3), 6.97-7.12 (m, 4H, Ph-*H*), 4.03 (s, 3H, OCH_3), 2.40 (s, 3H, CH_3) ppm. FT-IR (KBr): *v* 3431 (w), 3025 (m), 2953 (w), 2873 (w), 1625 (m), 1586 (m), 1569 (s), 1510 (m), 1474 (vs), 1425 (m), 1377 (m), 1297 (vs), 1238 (m), 1173 (m), 1098 (vs), 1011 (s), 957 (vs), 867 (w), 831 (s), 796 (s), 748 (w), 730 (m), 646 (m), 582 (m), 518 (m), 505 (w), 472 (w) cm^{-1}.

[ZnL_3Cl_2] (Zn3). L_3 (24.2 mg, 0.1 mmol) and $ZnCl_2$ (13.6 mg, 0.1 mmol) were refluxed in 25 mL of anhydrous methanol for 4 h. The mixture was then cooled to the room temperature and filtered. The filtrate was allowed to stand at room temperature in air. Yellow bulk crystals **Zn3** were obtained by slow evaporation after 18 days. Yield: 27.3 mg (72 %). Anal. Calcd for **Zn3** [$C_{14}H_{14}Cl_2N_2O_2Zn$ (378.56)]: C, 44.41; H, 3.73; N, 7.40 %. Found: C, 44.10; H, 3.87; N, 7.75 %. ^{1}H NMR (400 MHz, $CDCl_3$, 298K): δ 8.83 (s, 1H, C*H*=N), 8.03 (t, 1H, Py-H_5), 7.61 (d, 1H, Py-H_4), 7.45 (d, 1H, Py-H_3), 7.00-7.18 (m, 4H, Ph-*H*), 4.25 (s, 3H, Py-OCH_3), 4.15 (s, 3H, Ph-CH_3) ppm. FT-IR (KBr): *v* 3436(m), 3085 (w), 2946 (w), 2889 (w), 1620 (w), 1589 (m), 1571 (m), 1498 (s), 1481 (vs), 1433 (m), 1378 (s), 1306 (s), 1259 (vs), 1184 (m), 1093 (m), 1050 (w), 1024 (s), 1009 (s), 966 (s), 872 (w), 805 (s), 761 (s), 739 (m), 602 (w), 567 (w), 537 (w), 434 (w) cm^{-1}.

[CdL_3Cl_2] (Cd3). The procedure is similar to that of **Zn3**, except that $CdCl_2$ (22.8 mg, 0.1 mmol) was used instead of $ZnCl_2$. Yellow bulk crystals **Cd3** were obtained by slow evaporation after 1 days. Yield: 33.2 mg (78 %). Anal. Calcd for **Cd3** [$C_{19}H_{24}Cl_2N_2O_2Cd$ (425.57)]: C, 39.51; H, 3.32; N, 6.58 %. Found: C, 39.83; H, 3.17; N, 6.40 %. ^{1}H NMR (400 MHz, $CDCl_3$, 298K): δ 8.79 (s, 1H, C*H*=N), 8.05 (t, 1H, Py-H_5), 7.56 (d, 1H, Py-H_4), 7.45 (d, 1H, Py-H_3), 7.08-7.18 (m, 4H, Ph-*H*), 4.03 (s, 3H, Py-OCH_3), 3.85 (s, 3H, Ph-CH_3) ppm. FT-IR (KBr): *v* 3069 (w), 2950 (w), 2869

(w), 1621 (w), 1588 (m), 1567 (s), 1496 (s), 1474 (vs), 1427 (m), 1377 (s), 1304 (s), 1250 (s), 1165 (m), 1121 (w), 1100 (m), 1055 (w), 1007 (m), 960 (s), 868 (w), 800 (s), 757 (s), 741 (m), 658 (w), 596 (m), 536(w), 481 (w) cm^{-1}.

$[HgL_3Cl_2]$ (Hg3). The procedure is similar to that of **Zn3**, except that $HgCl_2$ (27.2 mg, 0.1 mmol) was used instead of $ZnCl_2$. Yellow bulk crystals **Hg3** were obtained by slow evaporation after 1 days. Yield: 37.0 mg (72 %). Anal. Calcd for **Hg3** [$C_{14}H_{14}Cl_2N_2O_2Hg$ (513.76)]: C, 32.73; H, 2.75; N, 5.45 %. Found: C, 32.47; H, 2.86; N, 5.53 %. ^{1}H NMR (400 MHz, $CDCl_3$, 298K): δ 8.79 (s, 1H, C*H*=N), 7.95 (t, 1H, Py-H_5), 7.56 (d, 1H, Py-H_4), 7.45 (d, 1H, Py-H_3), 6.97-7.10 (m, 4H, Ph-*H*), 4.16 (s, 3H, Py-OCH_3), 4.03 (s, 3H, Ph-CH_3) ppm. FT-IR (KBr): ν 3436 (m), 3072 (w), 2990 (w), 2839 (w), 1623 (w), 1587 (m), 1570 (m), 1498 (m), 1473 (s), 1422 (w), 1383 (m), 1293 (s), 1258 (s), 1179 (m), 1121 (w), 1092 (m), 1055 (w), 1024 (m), 1008 (m), 960 (s), 797 (s), 764 (s), 738 (m), 595 (m), 563 (w), 534 (w) cm^{-1}.

3. Result and Discussion

3.1. Synthesis and Characterization of Ligands and Complexes

Three new ligands ortho-(6-methoxy-pyridyl)(CH=NAr) (Ar = 2,6–iPr$_2$C$_6$H$_3$, **L_1**; 4–MeC$_6$H$_4$, **L_2**; 2–OMeC$_6$H$_4$, **L_3**) were synthesized by the condensation of 6-methoxy-2-pyridinecarboxaldehyde with the corresponding aniline in refluxing anhydrous methanol in the presence of a catalytic amount of formic acid (Scheme 1). All complexes **Zn1**–**Zn3**, **Cd1**–**Cd3** and **Hg1**–**Hg3** were self-assembled by the reaction of Zn(II)/Cd(II)/Hg(II) chloride and corresponding ligands at refluxing temperature. The formation of the schiff-base complexes can be rationalized in the light of template effect of Zn(II)/Cd(II)/Hg(II) modulated by the counter cations. A template agent (free ligand) can be said to contain the required structure to organized a collection of building blocks so that they can be linked together in a specific manner.[16] The identities of ligands and complexes are established by ^{1}H NMR, UV/Vis and FT-IR spectroscopies, and satisfactory elemental analysis data. The crude products of the ligands were recrystallized from *n*-hexane to give the pale yellow solid (**L_1**), yellow solid (**L_2**) and brown yellow oil (**L_3**), respectively. X-ray quality crystals of **Zn1**, **Zn3**, **Cd1**–**Cd3**, **Hg1** and **Hg3** were obtained by slow evaporation

methanol solution; **Zn2** and **Hg2** were obtained by slow evaporation methanol/dichloromethane solution. The yields of ligands and complexes are within the range 77%–89% and 45%–78%, respectively. We confirm that all the complexes are stable in the solid state upon extended exposure to air. All ligands have well solubility in common organic solvents and complexes are slightly soluble in very low polarity solvents, such as *n*-hexane, benzene and toluene, soluble in proton solvent and high polarity solvents, such as DMF and DMSO.

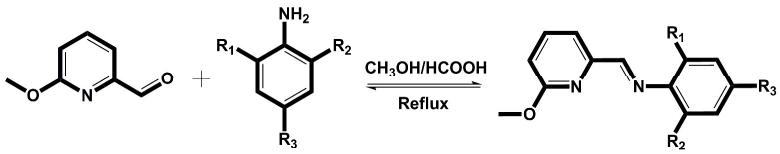

L_1 : R_1=R_2=*i*Pr, R_3=H
L_2 : R_1=R_2=H, R_3=Me
L_3 : R_1=OMe, R_2=R_3=H

Scheme 1 The synthetic procedure for ligands **L_1**–**L_3**.

The FT-IR spectra of ligands (**L_1**–**L_3**) and complexes (**Zn1**–**Zn3**, **Cd1**–**Cd3** and **Hg1**–**Hg3**) are shown in the Supporting Information (Fig. S1–S3). In the FT-IR spectra, the characteristic in-plane and out-of-plane deformation bands of the 2-substituted pyridine rings shift to higher frequencies [*ca*. 30 cm^{-1} δ(Py) and 20 cm^{-1} γ(Py)] in comparison with similar free ligands.[17] Several bands in the range 2800–3000 cm^{-1} are assigned to the pyridine ν_{C-H} stretching vibration. The appearance of a band in the region of 1620–1647 cm^{-1}, assigned to $\nu_{C=N}$, are slightly red-shifted by the range of 3–12 cm^{-1} relative to that of the free schiff-base ligand (1628–1647 cm^{-1}) upon coordination of the metal ions,[18] suggesting coordination through the schiff-base nitrogen atoms weakens the C=N double bonds. Extensive studies[19] have shown that the ***s*** character of the nitrogen lone pair in the –N bond increases upon coordination, producing a shorter C=N bond length and a greater –N stretching force constant (higher frequency of vibration). For all of ligands and complexes, three medium to strong peaks observed in the range 1570–1454 cm^{-1} are likely to be associated with the pyridine rings. The ν_{C-O} stretching vibration is observed in the range of 1222–1297 cm^{-1}. A medium to weak metal-sensitive stretching band in the 416–411 cm^{-1} range for all complexes can be assigned to the

$\nu_{(M–N)}$ vibration. These phenomena confirm the coordinative interaction between the nitrogen atoms and metal cations.

The ^{1}H NMR spectra of ligands and complexes have been recorded in $CDCl_3$ solutions to probe the solution structure (see the Supporting Information, Fig. S4–S6). The three protons on pyridine rings do not exhibit spin structure and display low field signals compared to phenyl protons, which appear as broad signal at *ca*. δ = 6.81–8.16. Further, a common trend in the position of these signals is that as all complexes were formed by the imine–N and pyridine–N displays a 0.01–0.75 ppm shift. This behavior causes a characteristic change of the sequence of chemical shift positions of the pyridine proton resonances compared to that in the free ligands. The ^{1}H NMR spectra of complexes (8.18–8.83 ppm) show that the resonances of the imine –C*H*=N– moiety protons shift toward low field compared to those of the corresponding ligands (8.18–8.50 ppm), indicating the formation of the coordination bonds between the ligand and the M(II) center.[20] For ligands and corresponding complexes, the obvious strong signal at *ca*. 3.99–4.27 ppm is assigned to the –OCH_3 group protons of pyridine rings. Especially for $\mathbf{L_1}$ and corresponding complexes (**Zn1**, **Cd1** and **Hg1**), appearance of protons of –C*H*– group as solitary signal unambiguously testified that the ligands and complexes are magnetically equivalent. The multiplet at the higher field in the range of 2.95–3.13 ppm is assigned to the –C*H*– group protons. For the corresponding complexes of $\mathbf{L_1}$–$\mathbf{L_3}$, differing only in the species of the methyl substituents on the phene ring, the methyl resonance is observed in the region 1.08–1.18, 2.02–2.42 and 3.85–4.15 ppm, respectively.

In order to confirm the phase purity of the bulk materials, powder X-ray diffraction (PXRD) experiments were carried out on nine complexes (**Zn1**–**Zn3**, **Cd1**–**Cd3** and **Hg1**–**Hg3**) (See the Supporting Information, Fig. S7). Although the experimental patterns have a few unindexed diffraction lines and some are slightly broadened in comparison with the simulated from the single crystal models, they still can be considered favorably that the bulk synthesized materials and the as-grown crystals are homogeneous for all complexes. The differences in intensity may be due to the preferred orientation of the crystalline powder samples.[21]

3.2. X-ray crystal structures

The eventual goal here is to investigate the possibility that the ultimate crystal morphology can be influenced by the metallic unit at the very beginning of the crystal growth process. In order to investigate the effect of different metal ions on the crystal structures, the metal salts with the different metal cations and the same anions, namely, $ZnCl_2$, $CdCl_2$ and $HgCl_2$ were used. Moreover, the ligands **L_1**, **L_2** and **L_3** were employed in order to study the influence of different electron donating substituents of the aniline on the construction of structures. Crystal data and experimental details for the crystals are summarized in Table 1, and selected bond lengths and bond angles are given in Table S1–S3. In zinc and mercury complexes, Zn(II) and Hg(II) formed tetrahedral complexes, while Cd(II) tends to form square pyramidal complexes, which can be observed from the crystal structures of **Cd1** and **Cd3**. In the nine complexes, the structures of ligand play important roles on the construction of complexes. The dihedral angles between the pyridine ring and phene ring in the complexes of **L_1**, **L_2** and **L_3** are in the range of 79.58(1)°–79.92(1)°, 7.65(2)°–11.12(2)° and 10.53(1)°–15.23(2)°, respectively (See the Supporting Information, Table S4). The $–OCH_3$ group in pyridine ring does not coordinate to the metal center in these complexes because of the stereospecific blockade. However, it can serve as the donor of hydrogen bonds and still play important roles in formation of supramolecular structures through C–H···Cl hydrogen bonds. Furthermore, in these complexes, there are more chances to form C–H···Cl hydrogen bonds (See the Supporting Information, Table S5) and π···π stacking interactions (See the Supporting Information, Table S6) between the ligands, which play significant roles in constructing the three-dimensional structures. All complexes are air stable and can retain their structural integrity at room temperature for a few months.

Structure of [ML_1Cl_2] (M = Zn, Zn1; Hg, Hg1). Single-crystal X-ray diffraction studies were performed on two dichloride complexes of ligand **L_1**. The complex **Hg1** is isostructural to **Zn1** and the structure of **Hg1** is shown in Fig. S8, ESI†. Herein, only the structure of **Zn1** will be discussed in detail. Complex **Zn1** crystallizes in the monoclinic system, space group $P2_1/c$. As shown in Fig. 1a, the zinc atom is

tetrahedral coordinated by two chlorine atoms and two nitrogen atoms derived from the clelating ligand $\mathbf{L_1}$. It is noteworthy that it gives rise to a five-membered ring after coordinated, which have coplanar with inherency of pyridine ring and indirectly results the extended conjugate. The mononuclear structure is indeed caused by the distorted dihedral angel between the pyridine ring and the phene ring. The dihedral angles between the pyridine ring and phene ring in the complexes **Zn1** (79.73(8)°) (Fig. 1b) and **Hg1** (79.92(1)°) are approximate perpendicular. The formal double-bond character of the imino linkage N2–C6 [C=N distance is 1.269 Å] is in compatible with the values of the previously published zinc complexes. The bond lengths of Zn–N1 (pyridine) and Zn–N2 (imine) are 2.069 and 2.112 Å, respectively, which is similar to the results from the literature reported previously.[22]

Furthermore, the H···Cl distance (2.896 Å) between the CH and the chlorine atoms from neighboring molecules is shorter than the sum of the van der Waals radii for H and Cl (*ca.* 1.2 Å for H, 1.75 Å for Cl),[23] and the C–H···Cl angle is 168.58°, which indicates a typical intermolecular hydrogen bonds. By linkage of the intermolecular hydrogen bonds, a one-dimensional chain structure is formed (Fig. 1c). In addition, π···π stacking interactions with centroid···centroid distances of 3.508 and 3.696 Å (Fig. 1d), respectively, provide further stability to the structure.

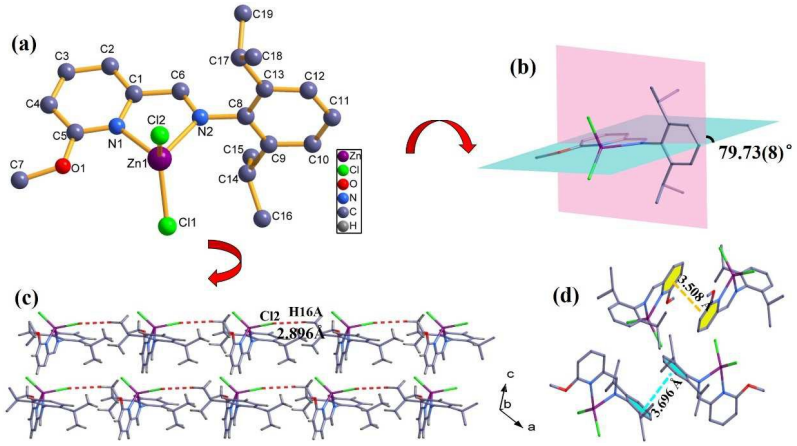

Fig. 1 (a) The structure unit of complex **Zn1**, H atoms omitted for clarity. (b) The picture of the dihedral angel between the pyridine ring and phene ring in complex **Zn1**. (c) The one-dimensional chain of complex **Zn1** formed by C–H···Cl hydrogen bonds. Dotted lines represent the weak interactions. (d) View of the π···π stacking interactions in complex **Zn1**.

Structure of $[CdL_1Cl_2]_2$ (Cd1). Complex **Cd1** crystallizes in the monoclinic

system, space group $P2_1/c$. The X-ray single-crystal structure of **Cd1**, shown in Fig. 2a, consists of half of the neutral dimer molecule, with the other half obtained by a centre of inversion. The dimer moiety contains two Cd(II) atoms (Cd1 and Cd1A), which are asymmetrically bridged by two chloride anions (Cl1 and Cl1A), while the molecule of the bidentate $\mathbf{L_1}$ ligand is *N*-coordinated to each cadmium atom. The separation of intramolecular Cd1···Cd1A is 3.779 Å. In the structure of complex **Cd1**, the coordination geometry around the cadmium atom is described as distorted square pyramidal ($\tau = 0.244$) [$\tau = (\beta-\alpha)/60°$, where α and β are the two largest angles in the coordination environment; $\tau = 0$ for a perfect square pyramid; $\tau = 1$ for an ideal trigonal bipyramid].[24] This is achieved by the basal coordination positions held by two atoms (N1 and N2) from the ligand $\mathbf{L_1}$ and two chlorine atoms (Cl1 and Cl1A) and the apical sites occupied by one chlorine atom (Cl2) (Fig. 2b). The bond angels around the Cd1 and Cd1A ions are in the range of 69.93(10)–153.03(8)° and 69.89(10)–157.02(8)°, respectively. The selected bond lengths and bond angles are given in Table S2, ESI†. Likewise the dihedral angle between the pyridine ring and phene ring in the complex **Cd1** (79.58(1)°) is approximate perpendicular due to the big steric hindrance of 2,6–iPr$_2$ substitute.

In the molecular packing structure of **Cd1**, C–H···Cl hydrogen bonds based on the chlorine atom and CH of the ligand are found, the distances of H···Cl and C–H···Cl angles are in the range of 2.730–2.915 Å and 121.77(1)–152.29(2)° (Table S5, ESI†), respectively. Meanwhile the π···π stacking interactions with centroid···centroid distances of 3.882 Å exist in the pyridine and pyridine ring. As shown in Fig. 3a, the neighboring dimer molecules are linked by intermolecular C–H···Cl hydrogen bonds to form a one-dimensional structure along the *b* axis. In the *bc* plane, the molecules are also interconnected by C–H···Cl hydrogen bonds to aggregate in a two-dimensional net (Fig. 3b). The two-dimensional nets further extend into three-dimensional supramolecular structures, as shown in Fig. 3c. In the structures of the complexes **Zn1**, **Cd1** and **Hg1**, the distances of M–N (imino) are relatively shorter than M–N (pyridine). The average distance of M–N bond is 2.091 Å (**Zn1**), 2.371 Å (**Cd1**), 2.422 Å (**Hg1**), respectively, which is consistent with ionic

radii. The bond angle of N–M–N is 78.89(8)° (**Zn1**), 69.93(10)° (**Cd1**) and 69.00 (12)° (**Hg1**), respectively.

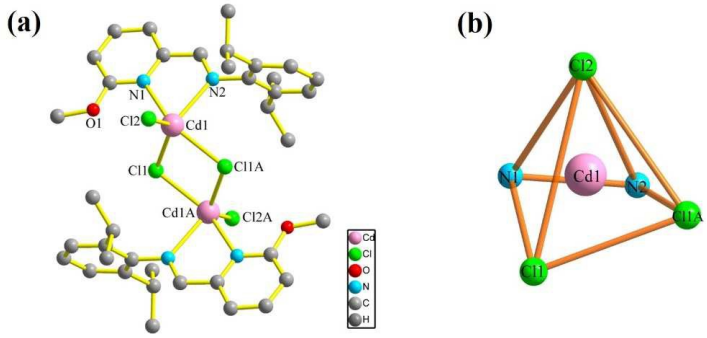

Fig. 2 (a) The structure unit of complex **Cd1**, H atoms omitted for clarity. (b) Polyhedral representation of the coordination sphere of the Cd(II) centre, with distorted square pyramid arrangement in the complex **Cd1**.

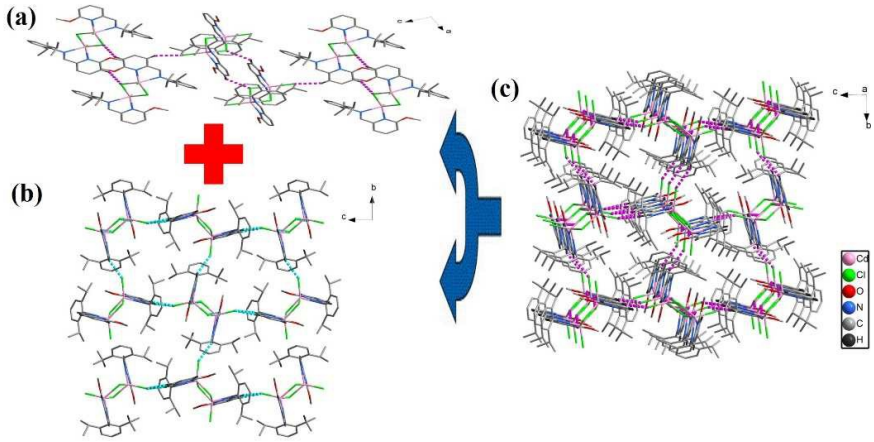

Fig. 3 (a) The one-dimensional chain of complex **Cd1** viewed along the [010] direction. (b) The two-dimensional structure of complex **Cd1** viewed along the [100] direction. (c) The three-dimensional structure of complex **Cd1** formed by C–H···Cl hydrogen bonds. Dotted lines represent the weak interactions.

Structure of [ML_2Cl_2] (M = Zn, Zn2; Cd, Cd2; Hg, Hg2). The complexes **Cd2** and **Hg2** are isostructural to **Zn2**, and their structures are shown in Fig. S9 and S10, ESI†. Thus, the structure description of **Zn2** is given in detail as a representative example. Complex **Zn2** belongs to the triclinic system, space group $P\bar{1}$. As shown in Fig. 4a, each Zn(II) center is four coordinated with a typically tetrahedron geometry (Fig. 4b). Each Zn(II) center is bidentately chelated by $\mathbf{L_2}$ via two nitrogen atoms (N1 and N2), and the remaining sites are occupied by two chlorine atoms (Cl1 and Cl2). The dihedral angle between the pyridine ring and phene ring is 11.12(2)° (**Zn2**), 9.91(9)° (**Cd2**) and 7.65(2)° (**Hg2**), respectively, which is approximate paralleled compared with the complexes of the ligand $\mathbf{L_1}$. Likewise the distances of M–N (imino)

are relatively shorter than M–N (pyridine). The average distance of M–N bond is 2.079 Å (**Zn2**), 2.288 Å (**Cd2**), 2.335 Å (**Hg2**), respectively, which is consistent with ionic radii. The N–M–N bond angles fall in the range of 71.60(3)–80.40(2)°, which are much smaller than the ideal bond angle of a sp^3 hybrid orbital (109.28°). The selected bond lengths and bond angles are given in Table S1, ESI†.

As shown in Fig. 4c, the chlorine atom of the $ZnCl_2$ is not playing a bridging effect, but it plays an important role in the formation of higher dimensional structures through C–H···Cl hydrogen bonds. The distances of H12A···Cl1, H6A···Cl2 and H14B···Cl2 are 2.858, 2.790 and 2.841 Å, respectively. The bond angles of C12–H12A···Cl1, C6–H6A···Cl2 and C14–H14B···Cl2 are 164.60°, 149.06° and 166.08°, respectively. These indicate the typical intermolecular hydrogen bonds between the neighboring molecules. In addition, there are weak π···π stacking interactions between pyridine ring and phene ring [the distance is 3.565 Å] in the crystal lattices of **Zn2** (Fig. 4d). By linkage of the intermolecular hydrogen bonds and π···π stacking interactions, a three-dimensional supramolecular structure is formed.

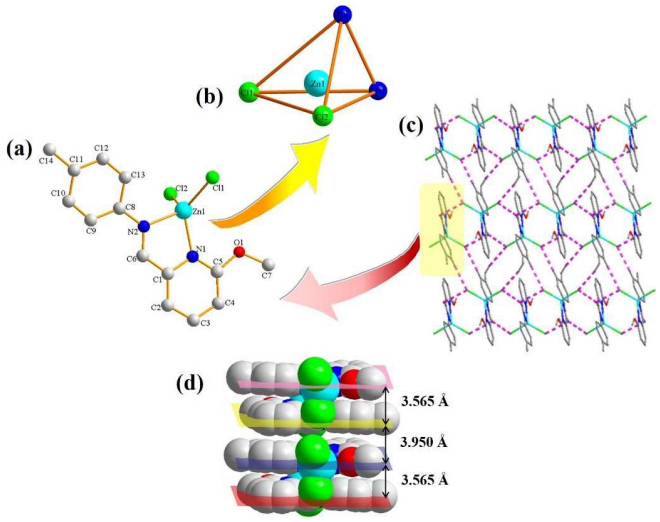

Fig. 4 (a) The structure unit of complex **Zn2**, H atoms omitted for clarity. (b) Polyhedral representation of the coordination sphere of the Zn(II) centre, with distorted tetrahedral arrangement in the complex **Zn2**. (c) The stack view of a two-dimensional structure generated by the C–H···Cl hydrogen bonds in **Zn2** along the [001] direction. (d) View of the π···π stacking interactions in **Zn2**.

Structure of [ML_3Cl_2] (M = Zn, **Zn3**; Hg, **Hg3**). The structures of **Zn3** and **Hg3** are isostructural to each other, therefore, **Zn3** is described here representatively. The

structure of **Hg3** is shown in Fig. S11, ESI†. X-ray crystallographic analysis reveals that **Zn3**, possessing a mononuclear structure, is a neutral complex crystallizing in a monoclinic system, space group $P2_1/c$ (Fig. 5a). The asymmetric unit consists of one Zn(II) atom, one $\mathbf{L_3}$ ligand and two chlorine ions. Each Zn(II) atom is located in a distorted tetrahedral coordination environment, provided by two nitrogens ($N_{pyridine}$ and N_{imine}) and two chlorines. Moreover, it is raised a new five-membered ring, which have coplane with the pyridine ring. The average distance of M–N bond is 2.156 Å (**Zn3**) and 2.408 Å (**Hg3**), respectively, which is consistent with ionic radii. The bond angle of N–M–N is 78.60(2)° (**Zn3**), and 69.36 (18)° (**Hg3**), respectively. The selected bond lengths and bond angles are given in Table S1, ESI†. The parameters of bond length and angle are close to the values of related Zn(II)/Hg(II) complexes. Likewise the dihedral angles between the pyridine ring and phene ring in the complexes **Zn3** (15.23(2)°) and **Hg3** (12.22(1)°) are approximate paralleled due to the small steric hindrance of 2–OCH_3 substitute. In complex **Zn3**, ligand $\mathbf{L_3}$ utilizes its two nitrogen atoms ($N_{pyridine}$ and N_{imine}) to ligate Zn(II) atom. The mononuclear unit are further linked by intermolecular C–H···Cl hydrogen bonds to form supramolecular structure. The distances of H···Cl and C–H···Cl angles are in the range of 2.884–2.943 Å and 115.81(4)–150.39(5)° (Table S5, ESI†), respectively. Meanwhile the π···π stacking interactions with centroid···centroid distances of 3.706 Å exist in the pyridine and phene ring. As a result, by the linkage of such intermolecular hydrogen bonds and π···π stacking interactions, a three-dimensional supramolecular structure is formed (Fig. 5b).

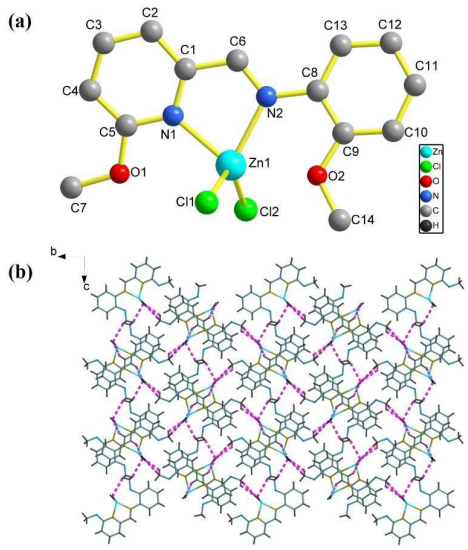

Fig. 5 (a) The structure unit of complex **Zn3**, H atoms omitted for clarity. (b) The three-dimensional structure of complex **Zn3** formed by C–H···Cl hydrogen bonds. Dotted lines represent the weak interactions.

Structure of [CdL_3Cl_2] (Cd3). For **Cd3**, the X-ray single-crystal structure, shown in Fig. 6a, consists of one $\mathbf{L_3}$ ligand and two coordinated chlorine ions. The coordination geometry around the cadmium atom is five-coordinated in a distorted square pyramid (Fig. 6b) with the value of τ being 0.122. One oxygen atom (O2) and two nitrogen atoms (N1 and N2) from $\mathbf{L_3}$ and one chlorine atom (Cl1) are ligated to the Cd(II) center in the equatorial plane, with another chlorine atom (Cl2) located in the axial position. The distance of the apical chlorine atom to the metal center is longer than that of the basal chlorine atom. The distance of Cd–N1, Cd–N2, Cd–O2 are 2.333, 2.344 and 2.517 Å, in agreement with the values of a similar Cd(II) complexes. The selected bond lengths and bond angles are given in Table S3, ESI†. In complexes **Zn3**, **Cd3** and **Hg3**, Zn(II) and Hg(II) ions adopt four-coordination mode , but Cd(II) ion shows five-coordination mode. As aforementioned, although the complexes **Zn3**, **Cd3** and **Hg3** use the same ligand, the results reveal that the ligand $\mathbf{L_3}$ can selectively chelate the Zn(II), Cd(II) and Hg(II) metal ions, which may be rationalized by the cooperative effect of the radius and the coordination preferences of the metal ions. Similar to complex **Zn3**, intermolecular C–H···Cl hydrogen bonds between the CH of the ligand and chlorine atoms are observed. The distances of H···Cl and C–H···Cl angles are in the range of 2.775–2.934 Å and

116.34(3)–152.42(3)° (Table S5, ESI†), respectively, which lie in the normal range as previously reported. Meanwhile the π···π stacking interactions with centroid···centroid distances of 3.423 and 3.574 Å (Table S6, ESI†), respectively, provide further stability to the structure. Finally, three-dimensional supramolecular structure is formed (Fig. 6c).

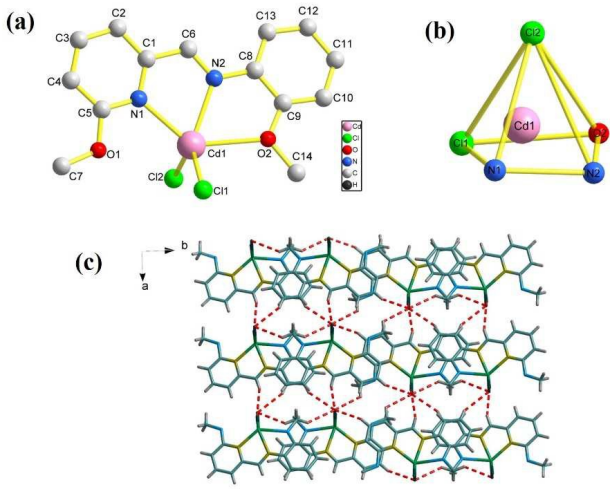

Fig. 6 (a) The structure unit of complex **Cd3**, H atoms omitted for clarity. (b) Polyhedral representation of the coordination sphere of the Cd(II) centre, with distorted square pyramid arrangement in the complex **Cd3**. (c) The stack view of a two-dimensional structure generated by the C–H···Cl hydrogen bonds in **Cd3** along the [001] direction.

Nine complexes were prepared by the coordination of the ligands **L_1**–**L_3** with d^{10} metal ions Zn(II), Cd(II) and Hg(II), meanwhile there are some similarities and differences in their structures. On one hand, the persistent trend in series of structures reported herein is the presence of chelating ortho-(6-methoxy-pyridyl)(CH=NAr) ligands and the observation that the M–N(imino) bond length is consistently longer than the M–N(pyridine) bond length (Δ(M–N) = 0.04 to 0.14 Å, except for **Cd3** where it is only 0.01 Å). In general, the above mentioned Δ(M–N) values increase according to the order of the periodic table. The overall molecule of ligand is planar as seen in the dihedral angle of 7.65(29)–79.92(13)° formed between the pyridine and phene ring planes, and the coordinated chlorine atoms are located up and down the plane. Across the series, the M–N–C bond angles follow the same trends with *exo*-chelate ring angles are wider than the *endo*-chelate ring angles (Table S1–S3, ESI†). On the other hand, the coordination number of center metal reveals that the ligands can

selectively chelate the Zn(II), Cd(II) and Hg(II) metal ions, which may be rationalized by the cooperative effect of the radius and the coordination preferences of the metal ions. Zn(II)/Hg(II) tend to form tetrahedral complexes, while Cd(II) tends to form square pyramidal complexes, which can be observed from the crystal structures of **Cd1** and **Cd3**. In summary, the diverse complex structures were obtained thanks to the structure and coordination site of the ligand, in combination with different metal atoms.

3.3. Photophysical properties

Table 2 summarizes the absorption data of the free ligands $\mathbf{L_1}$–$\mathbf{L_3}$ and complexes **Zn1**–**Zn3**, **Cd1**–**Cd3** and **Hg1**–**Hg3** in acetonitrile solution at 298 K. The electronic absorption spectra of $\mathbf{L_1}$–$\mathbf{L_3}$ in acetonitrile displayed in the range 300–353 nm that were derived from the π–π* transitions, originating from the phene and pyridine group (see the Supporting Information, Fig. S12). The absorption spectra of **Zn1**–**Zn3**, **Cd1**–**Cd3** and **Hg1**–**Hg3** are bathochromically shifted (300–385 nm) to those of the corresponding schiff-base ligand $\mathbf{L_1}$–$\mathbf{L_3}$, for the metal perturbed intraligand π–π* transition of the imine(pyridine) unit.[25] The molar extinction coefficients of the complexes are in the range from 10219 to 54004 $dm^3\ mol^{-1}\ cm^{-1}$. For the complexes of the same ligand, the absorption spectra shows the blue shift with decreasing absorption intensity according to the order of the periodic table (Zn > Cd > Hg). It is very interesting that the electron-donating ability of substituent groups ($–OCH_3$ > $–CH_3$ > –*i*Pr) in aniline plays a crucial role in governing the absorption band energies. The energy trend is found to follow the order **Zn1** > **Zn2** > **Zn3** (as well as **Cd1**–**Cd3** and **Hg1**–**Hg3**).

The photophysical properties of these complexes revealed a striking metal-ion (Zn, Cd, Hg), ligand ($\mathbf{L_1}$, $\mathbf{L_2}$, $\mathbf{L_3}$), state of aggregation (solution and the solid state) and temperature dependence (298 K and 77 K). The emission energy of each ligand and complex is given in Table 2 and Table 3. In the degassed acetonitrile (CH_3CN) solution (1.0×10^{-5} mol L^{-1}) at 298 K, the maximum emissions of **Zn1**–**Zn3** are 406, 415 and 423 nm (408, 427 and 450 nm for **Cd1**–**Cd3**; 402, 418 and 430 nm for **Hg1**–**Hg3**). It is showed a bathochromic shift compared to that of the free ligand (400, 411 and 421 nm for $\mathbf{L_1}$–$\mathbf{L_3}$) and produce blue emission (Commission Internacionale d'Eclairage (CIE) coordinates alight on the blue region.) (see Fig. 7). These luminescence emissions are all attributable to the ligand-centered π*–π transitions.[26]

The maximum emission wavelength trend in the order **Zn3** > **Zn2** > **Zn1** (as well as **Cd1**–**Cd3** and **Hg1**–**Hg3**) is observed, in accord with the electron-donating ability of substituent groups in aniline. At 77 K, the emissions are red shifted obviously to green region and the largest shift is 168 nm for complex **Zn3** in CH_3CN (CIE: 0.47, 0.51). The corresponding maximum emission bands of **Zn1**–**Zn3** are observed at 494, 531 and 591 nm in CH_3CN (489, 510 and 576 nm for **Cd1**–**Cd3**; 489, 529 and 545nm, for **Hg1**–**Hg3**) (Fig. 13, ESI†). We consider the red shift at low temperatures most likely caused by the increased rigidity of the molecule at low temperatures and reduced by the intermolecular interaction.[27]

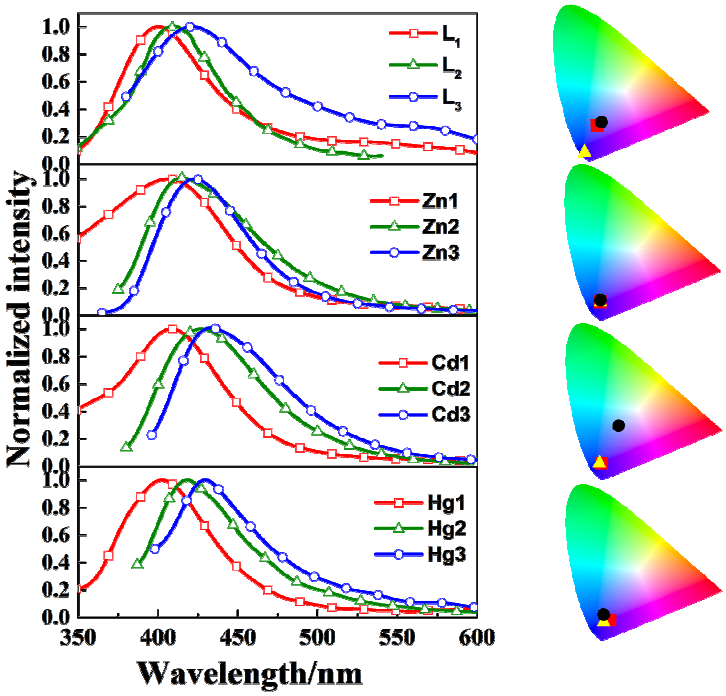

Fig. 7 Emission spectra of free ligands L_1–L_3 and complexes **Zn1**–**Zn3**, **Cd1**–**Cd3** and **Hg1**–**Hg3** in acetonitrile solution at 298 K and the corresponding color coordinate diagram of emission (square red = L_1, **Zn1**, **Cd1** and **Hg1**; triangle yellow = L_2, **Zn2**, **Cd2** and **Hg2**; circle black = L_3, **Zn3**, **Cd3** and **Hg3**).

The quantum yields of all ligands and complexes have been determined in acetonitrile solution at 298 K (Table 2). It was found that the quantum yields of complexes are higher than those of the free ligands. Particularly, the quantum yields of **Zn3** (Φ_F = 0.422) is 8.79-fold to L_3 ligand (Φ_F = 0.048). This is because the M(II) centers in complexes play a significant role in enhancing the ligand-centered π*–π fluorescent emission. The chelation of the ligand to metal center could increase the rigidity of the ligand, and reduces the loss of energy by thermal vibrational decay. Meanwhile, luminescence quantum yields decrease according to the order of the periodic table (Zn > Cd > Hg) when fix on the same ligand. The lowest luminescence

quantum yields of complexes **Hg1**–**Hg3** can be attributed to the "heavy atom effect".[28] The sensitivity of the luminescence intensity toward Hg(II) ions made us interested in the possibility application on luminescent sensor for Hg(II) ions. For the **Zn1**, **Zn2** and **Zn3** (Φ_F = 0.422, **Zn3** > 0.197, **Zn2** > 0.060, **Zn1**) complexes, the steric configuration and the electron donating nature resolve the luminescence properties together. Simultaneously, **Cd1**–**Cd3** and **Hg1**–**Hg3** also possess the same regularity.

At 298 K, the emission spectra of **M1**–**M3** (M =Zn, Cd and Hg) and $\mathbf{L_1}$–$\mathbf{L_3}$ in the solid state are shown in Fig. 8. In solid state all complexes emit green luminescence at λ_{max} = 509–543 nm when irradiated at 365 nm (Fig. 9). From the column charts of luminescence intensity (Fig. 10), we found the luminescence emission intensity of the complexes decrease according to the order of the periodic table (Zn > Cd > Hg) accompanied by the electron donating nature (–OCH_3 > –CH_3 > –*i*Pr), which is consistent with the regular pattern in CH_3CN solution. The zinc complexes show bright green luminescence and the difference in the intensity of the emission results from the variation of the coordinated central metals to $\mathbf{L_1}$–$\mathbf{L_3}$ ligands and indicates that the central metals strongly affect the luminescence emission features. In the solid state at 298 K, the maxima emission peaks for nine complexes are red shift ~100 nm compared with those in solutions of acetonitrile, which may be due to the formation of C–H···Cl hydrogen bonds and π···π stacking interactions in the solid state, which can effectively decrease the HOMO–LUMO energy gap, and influence the ligand-centered π*–π transitions.[29] Meanwhile, we investigate the solid state emission spectra of ligands and complexes at 77K, the details of emission spectra are shown in Table 3. The complexes emit intensely at the range of 488–557 nm, giving light with CIE coordinates of 0.23–0.39, 0.31–0.59, which are at the green light region. Compared with that at 298 K, the luminescence emission intensity of the complexes have the same change trend (Fig. 14, ESI†).

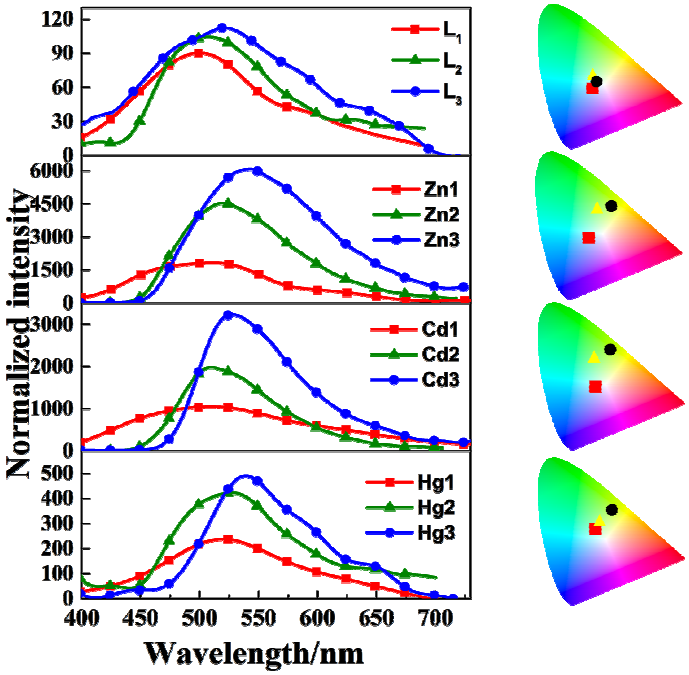

Fig. 8 The solid state emission spectra of free ligands $\mathbf{L_1}$–$\mathbf{L_3}$ and complexes **Zn1**–**Zn3**, **Cd1**–**Cd3** and **Hg1**–**Hg3** at 298 K at same testing condition (λ_{ex} = 365 nm, slit width: 1 nm, 1 nm) and the corresponding color coordinate diagram of emission (square red = $\mathbf{L_1}$, **Zn1**, **Cd1** and **Hg1**; triangle yellow = $\mathbf{L_2}$, **Zn2**, **Cd2** and **Hg2**; circle black = $\mathbf{L_3}$, **Zn3**, **Cd3** and **Hg3**).

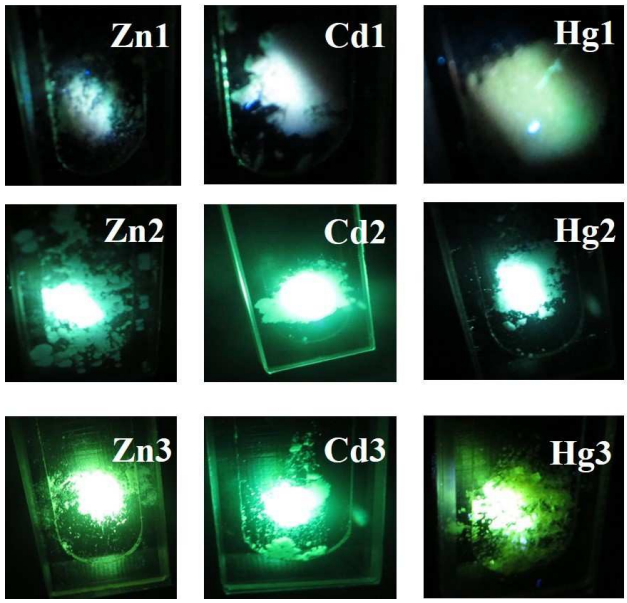

Fig. 9 Photographs of complexes **Zn1**–**Zn3**, **Cd1**–**Cd3** and **Hg1**–**Hg3** at same testing condition (λ_{ex} = 365 nm, slit width: 5 nm, 5 nm).

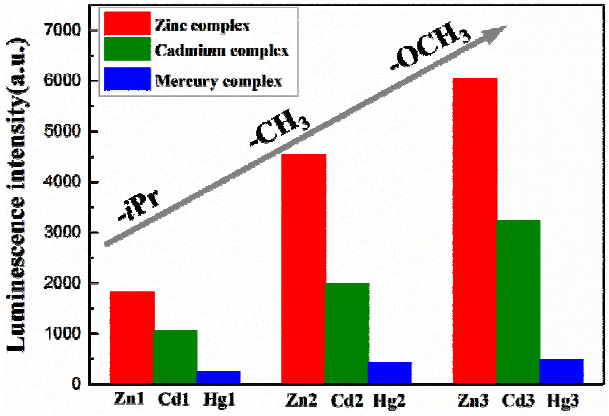

Fig. 10 Luminescence intensity of complexes **Zn1**–**Zn3**, **Cd1**–**Cd3** and **Hg1**–**Hg3** in the solid state at same testing condition (λ_{ex} = 365 nm, slit width: 1 nm, 1 nm).

As mentioned above, in the complexes **M1**–**M3** (M =Zn, Cd and Hg), the zinc complexes have maximum emission intensity and luminescence quantum yields in solid state and solution. This indicates the central metal and the structure of ligand affect the luminescence properties. Then, in order to investigate the influence of the external environment on the luminescence properties, we chose complex **Zn3** as an example to give some luminescence measurements in acetonitrile solution at different temperatures (from 298 K to 343 K). The thermal quenching of luminescence is an important technological parameter for materials because it has considerable influence on the light output.[30] The temperature-dependent luminescent properties of **Zn3** exited by 375 nm are presented in Fig. 11. With increasing the temperature, the maximum emission wavelength remains basically unchanged and the full width at half-maximum (FWHM) of the emission band increases from 57.5 to 59.9 nm. Curves A and B in the inset of Fig. 11 represent the temperature dependence of the integrated emission intensity and the emission peak height normalized with respect to the values at room temperature (298 K), respectively. When the temperature increases to 343 K, the normalized integrated emission intensity and emission peak height are found to be 75% and 73% of the values at 298 K, respectively. These phenomena can be explained by the interaction between the electron and thermally active phonon. The excited luminescent center is thermally activated through phonon interaction, and then thermally released through the crossing point between the excite state and the ground state. This nonraditive transition probability by thermal activation is strongly

dependent on temperature resulting in the decrease of emission intensity. The thermally activated luminescent center is strongly interacted with thermally active phonon, contributing to FWHM of emission spectrum. At higher temperature, the population density of phonon is increased, and the electron–phonon interaction is dominant, and consequently FWHM of emission spectrum is broadened.[31]

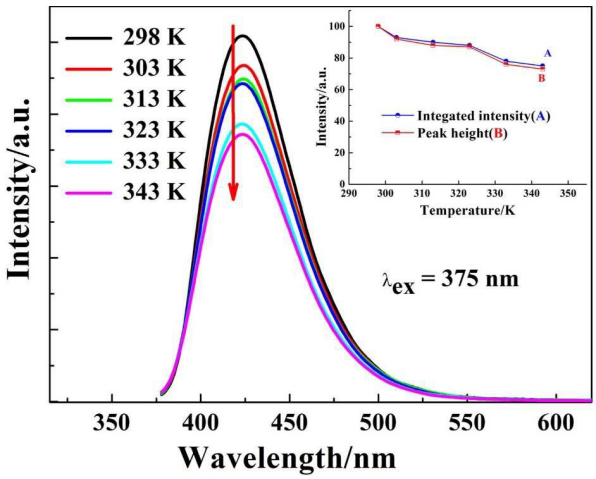

Fig. 11 The acetonitrile solution emission spectra of **Zn3** at different temperatures from 298 K to 343 K under excitation at 375 nm; inset shows temperature dependence of the integrated emission intensity (curve A) and the emission peak height (curve B) of **Zn3**.

Hence, we discovered that the luminescence emission intensities and wavelengths of coordination complexes with d^{10} metal centers can be easily tuned by each of the following factors: central metal, state of aggregation, solvent, and temperature. The results lead to conclusion that subtle changes in the structure of the ligand and the central metal give rise to significant differences in the structure of their coordination complexes, which will generate dramatic changes in their functional properties.

The luminescence decay profiles of ligands $\mathbf{L_1}$–$\mathbf{L_3}$ and complexes **Zn1**–**Zn3**, **Cd1**–**Cd3** and **Hg1**–**Hg3** were measured at their optimal excitation wavelengths in the solid state and acetonitrile solution at 298 K and 77K. The detailed data are listed in Table S7 and S8, ESI†. A general trend is that the luminescence lifetimes for M(II) (M = Zn, Cd and Hg) complexes either in the solid state or acetonitrile solution at 298 K and 77K are mostly longer than that of the corresponding ligands $\mathbf{L_1}$–$\mathbf{L_3}$. The most obvious observation is that the lifetime of **Zn3** (τ = 13.33 μs) is 2.55-fold to the corresponding ligand $\mathbf{L_3}$ (τ = 5.22 μs) in acetonitrile solution. This is attributed to the

more stable structure and interaction upon coordination.[32] Meanwhile, the luminescence lifetimes of the ligand and corresponding complexes in the solid state are longer than those in acetonitrile solution, which can be ascribed to the less polar nature of the environment in solid state.[33] The luminescence lifetimes of complexes **Hg1**–**Hg3** (8.82–14.95 μs at 298 K; 6.39–9.45 μs at 77 K) are shorter than that of **Zn1**–**Zn3** (11.41–19.82 μs at 298 K; 7.62–14.27 μs at 77 K) and **Cd1**–**Cd3** (10.79–15.37 μs at 298 K; 6.53–10.75 μs at 77 K), which may be a result of the heavy-atom effect of the Hg(II) ion.[34] Luminescence lifetimes for ligands and complexes at 298 K are mostly longer than that at 77 K, which are observed in Table S7 and S8, ESI†. This phenomenon can be attributed to the quenching of the center metal cation at a lower temperature. It should be pointed out that the lifetime of **Zn3** (τ = 19.82 μs) is longer than that of other complexes.

3.4. Application in DSSCs

The complexes **Zn1**–**Zn3** have the highest luminescence quantum yields compared to the corresponding other metal complexes. Meanwhile, the absorption of **Zn1**–**Zn3** are all in the region of 300–450 nm (Fig. S15, ESI†), which could compensate for that of N719 in the low wavelength region of the visible spectrum. Besides optical properties discussed above, energy-level matching is a crucial factor in selecting sensitizer. The HOMO and LUMO energy levels of **Zn1**, **Zn2** and **Zn3** were investigated by cyclic voltammetry (CV) measurement in a three-electrode cell and an electrochemistry workstation. The experimental data are summarized in Table 4. As estimated from the intersection of absorption and emission spectra, the excitation transition energy ($E_{0\text{-}0}$) of **Zn1**, **Zn2** and **Zn3** are 3.04, 3.01 and 2.94 eV, respectively. The HOMO value of **Zn1**, **Zn2** and **Zn3** corresponding to their first redox potential are -5.18, -4.86 and -5.02 eV, respectively. The estimated excited-state potential corresponding to the LUMO levels of **Zn1**, **Zn2** and **Zn3**, calculated from $E_{HOMO} + E_{0\text{-}0}$, are -2.14, -1.85 and -2.08 eV, respectively.[35] For better electron injection, this LUMO level should lie above the conduction band (CB) of the TiO_2 semiconductor (-4.40 eV vs vacuum) and for effective dye regeneration, the HOMO energy level should lie below the I^-/I_3^- redox electrolyte (-4.60 eV vs vacuum) which is further improved negatively about

0.3 V by adding additives such as 4-tert-butyl pyridine (TBP) to the I^-/I_3^- redox electrolyte.[36] This gives sufficient driving force for dye regeneration.[37] It shows that the energy levels of **Zn1**, **Zn2** and **Zn3** are appropriate for the DSSCs system containing TiO_2 (Fig. 12). Thus the complexes **Zn1**–**Zn3** were employed as co-sensitizer in photoanodes to prepare ZnX/N719 co-sensitized DSSCs devices.

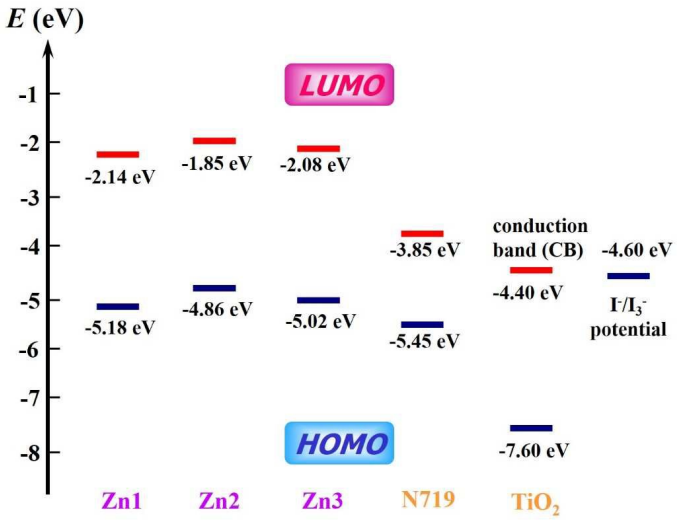

Fig. 12 Energy level diagrams of HOMO and LUMO for dyes from electrochemical data.

The current-voltage (*J*-*V*) characteristic of the DSSCs based on N719, **Zn1**/N719, **Zn2**/N719 and **Zn3**/N719 are shown in Fig. 13 and the corresponding cell performances are summarized in Table 4. The results show that, upon co-sensitization, the performances of cells are all improved. The values of J_{sc}, V_{oc} and η are improved in the order of **Zn3**/N719 > **Zn2**/N719 > **Zn1**/N719 > N719, respectively. The individually N719 sensitized device was found to exhibit η value of 5.11% (with J_{sc} = 11.19 mA/cm^2, V_{oc} = 0.70 V and FF = 0.65), while the co-sensitized solar cell devices **Zn1**/N719, **Zn2**/N719 and **Zn3**/N719 showed η value of 5.63% (with J_{sc} = 13.88 mA/cm^2, V_{oc} = 0.69 V and FF = 0.58), 6.35% (with J_{sc} = 14.81 mA/cm^2, V_{oc} = 0.71 V and FF = 0.60), and 6.94% (with J_{sc} = 16.59 mA/cm^2, V_{oc} = 0.72 V and FF = 0.58), respectively (Table 5). All the parameters are significantly higher than that of DSSCs sensitized by single N719.

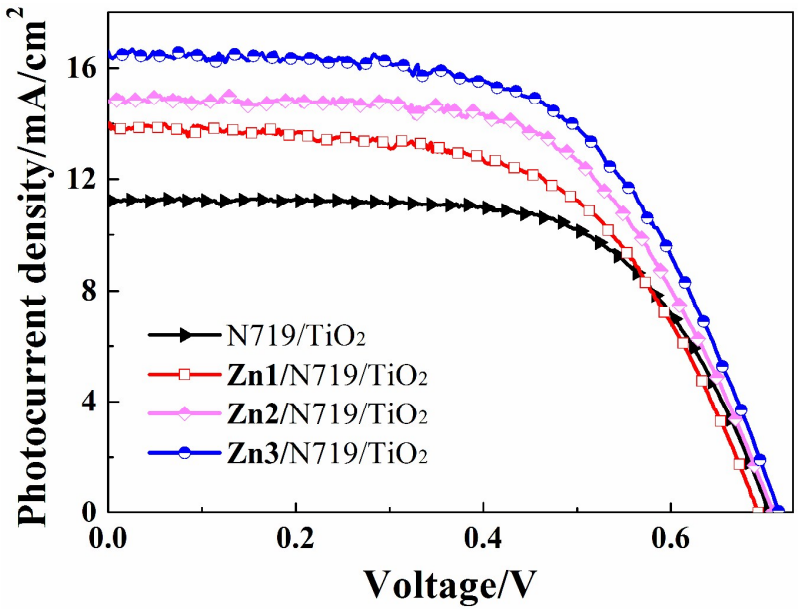

Fig. 13 *J-V* curves for DSSCs based on co-sensitized photoelectrodes and N719 sensitized photoelectrode under irradiation of 100 mW cm^{-2} AM 1.5G solar.

EIS is a powerful technique for the analysis of interfacial electronic and ionic transport processes in an electrochemical device.[38] It is a steady state method to measure current response based on application of an ac voltage at different frequencies. Herein, we utilized EIS to analyze charge carrier dynamics in the interfacial regions of solid-liquid layers. The Nyquist plots of EIS for DSSCs based on different photoelectrode were measured under standard global AM1.5 solar irradiation applying a forward bias of -0.75V. The three semicircles located in high, middle and low frequency regions (left to right) are attributed to the electrochemical reaction at the Pt/electrolyte interface, the charge transfer at the TiO_2/dye/electrolyte interface and a Warburg diffusion process of the I^-/I_3^- in the electrolyte.[39] Under light illumination, EIS was utilized to analyze the charge transport resistance at the TiO_2/dye/electrolyte interface for its significance on the efficiency of DSSCs.[40] As shown in Fig. 14, the radius of the large semicircle located in middle frequency regions in the Nyquist plot decrease after co-sensitized with zinc complexes, and the values are in the order of **Zn3**/N719 < **Zn2**/N719 < **Zn1**/N719 < N719, which indicates a decrease of the electron transfer impedance (R_{ct}) and a increase of charge transfer rate at this interface after co-sensitization. This is benefit for the enhancement of DSSCs performance.

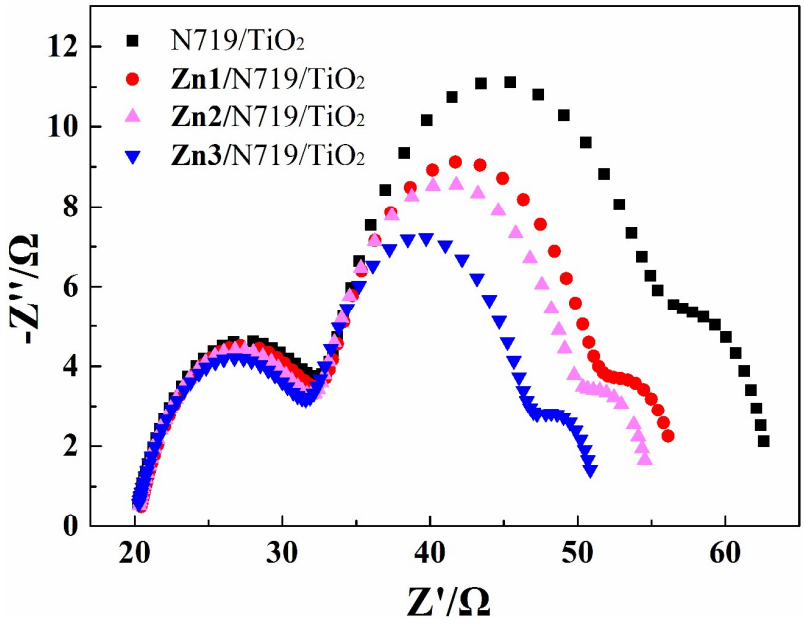

Fig. 14 Nyquist plots of EIS for DSSCs based on different photoelectrodes measured under standard AM 1.5G solar irradiation at forward bias -0.75V.

Dark current measurement of DSSCs has been considered as a qualitative technique to describe the extent of the back electron transfer.[35] A comparison of dark current between the investigated cells can provide useful information regarding the back electron transfer process. Fig. 15 shows the dark current–voltage characteristics of the DSSCs based on different photoelectrodes with the applied bias from 0 to +0.80 V. The onset of the dark current for individual N719 sensitized DSSC occurs at a bias about +0.30 V, with a subsequent dramatic increase of dark current with the increase of potential. In contrast, for the co-sensitized DSSCs, the onset potential shifted to about +0.45 V; furthermore, the dark current of the co-sensitized DSSCs increased much slower than that of N719 sensitized DSSC when potential was greater than +0.45 V. In other words, under the same potential bias, when the potential was $\geqslant$ 0.45 V, the dark current for the co-sensitized DSSCs was noticeably smaller than that for the N719 sensitized DSSC. The increase of the onset potential and the reduction of the dark current demonstrated that **Zn1**, **Zn2** and **Zn3** successfully suppress the electron back reaction with I_3^- in the electrolyte. This is critical to enhance the efficiency of DSSCs.

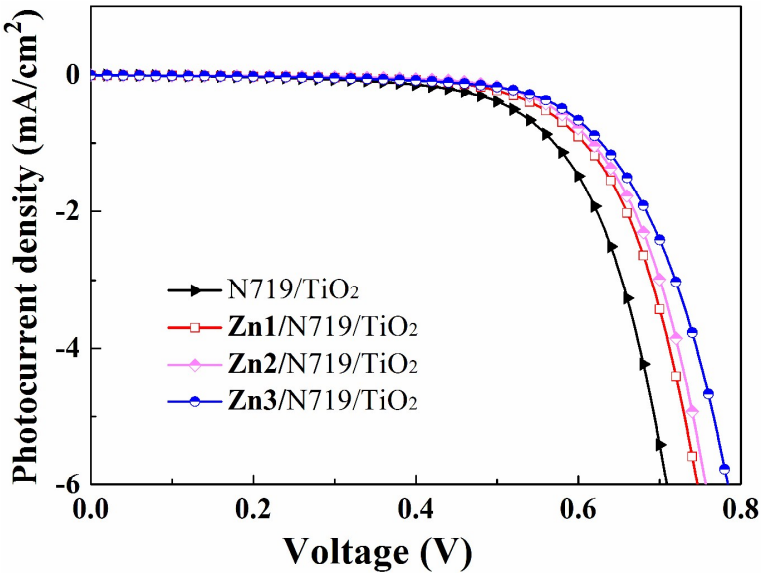

Fig. 15 *J-V* curves for DSSCs based on co-sensitized photoelectrodes and N719 sensitized photoelectrode in dark.

When the molecular structures of **Zn1**–**Zn3** are taken into account, it is found that introduction of electron-donating substituent group in aniline also has some effect on the performance of DSSCs. The enhancement of co-sensitized DSSCs performance compared with that of single N719 sensitized DSSCs is in the order of **Zn3**/N719 > **Zn2**/N719 > **Zn1**/N719 > N719. This indicates that the η value shows increasing according to the electron-donating ability of substituent groups (–OCH_3 > –CH_3 > –*i*Pr) in aniline. For introduction of –OCH_3 substituent the absorption shows a red shift and largest molar extinction coefficient (Table 4). The longer wavelength shift is better for compensating the absorption of N719 and overcoming the competitive light absorption of I_3^-. What's more, the dihedral angle between the pyridine ring and phene ring is 15.23(2)° (**Zn3**) is approximate paralleled. The good co-planarity is better for electronic energy transfer. Therefore, the performance of co-sensitized cell is in the order of **Zn3**/N719 > **Zn2**/N719 > **Zn1**/N719 > N719.

4. Conclusions

In summary, nine new transition metal (M = Zn, Cd and Hg) complexes with ortho-(6-methoxy-pyridyl)(CH=NAr) ligands were synthesized, characterized and their luminescent properties were studied. Crystal structure analysis reveals that M(II) (M = Zn, Cd and Hg) complexes adopt distorted tetrahedron geometry (except for

Cd1 and **Cd3**, which they display distorted square pyramid geometry) and have C–H···Cl hydrogen bonds and π···π stacking interactions in the solid-state. The series of complexes exhibit tunable luminescence from blue, green to light yellow by varying the temperature (298 K and 77 K) in the solution and in the solid state. The complexes **Zn1**–**Zn3** exhibit brighter luminescence in the nine transition metal complexes. The luminescence emission intensities of coordination complexes with d^{10} metal centers can be easily tuned by center metal or structure of ligand. Subtle changes in the structure of the ligand or the center metal give rise to significant differences in the structure of their coordination complexes, which will generate dramatic changes in their functional properties. The complexes **Zn1**–**Zn3** were employed as co-sensitizer in photoanodes to assemble with counter electrodes and electrolyte to prepare ZnX/N719 co-sensitized DSSCs devices. The results show that, upon co-sensitization, the performances of cells are all improved. In particular, the **Zn3**/N719 device exhibited a higher J_{sc} of 16.59 % mA/cm^2, corresponding to a overall conversion efficiency of 6.94%, which is *ca*. 36 % higher than that of devices sensitized by single N719, indicating that these complexes possess a wonderful potential in application of DSSCs.

Acknowledgements

This work was supported by National Natural Science Foundation of China (Grant 21371040 and 21171044), the National key Basic Research Program of China (973 Program, No. 2013CB632900), Supported by the Fundamental Research Funds for the Central Universities (Grant No. HIT. IBRSEM. A. 201409), and Program for Innovation Research of Science in Harbin Institute of Technology (PIRS of HIT No. A201416 and B201414).

Notes and references

1 (a) L. Sun, G. Z. Li, M. H. Xu, X. J. Li, J. R. Li and H. Deng, *Eur. J. Inorg. Chem.*, 2012, 1764; (b) S. M. Humphrey and P. T. Wood, *J. Am. Chem. Soc.*, 2004, **126**, 13236; (c) A. Galet, A. B. Gaspar, G. Agusti, M. C. Munoz, G. Levchenko and J. A. Real, *Eur. J. Inorg. Chem.*, 2006, 3571; (d) P. D. Harvey and D. Fortin, *Coord. Chem. Rev.*, 1998, **171**, 351; (e) L. Prodi, F. Bolletta, M. Montalti and N. Zaccheroni, *Coord. Chem. Rev.*, 2000, **205**, 59; (f) K. J. Franz, N. S. Bernhard, B. Spingler and S. J. Lippard, *Inorg. Chem.*, 2000, **39**, 4081; (g) P. S. Weiss, *J. Am. Chem. Soc.*, 2010, **132**, 10954.

2 (a) M. J. Vitorino, T. Devic, M. Tromp, G. Ferey and M. Visseaux, Macromol. *Chem. Phys.*, 2009, **210**, 1923; (b) S. Haneda, Z. B. Gan, K. Eda and M. Hayashi, *Organometallics*, 2007, **26**, 6551; (c) K. Yu, B. B. Zhou, Y. Yu, Z. H. Su and G. Y. Yang, *Inorg. Chem.*, 2011, **50**, 1862; (d) A. Dolbecq, E. Dumas, C. R. Mayer and P. Mialane, *Chem. Rev.*, 2010, **110**, 6009; (e) Y. Y. Li, C. K. Lin, G. L. Zheng, Z. Y. Cheng, H. You, W. D. Wang and J. Lin, *Chem. Mater.*, 2006, **18**, 3463.

3 (a) Q. K. Liu, J. P. Ma and Y. B. Dong, *J. Am. Chem. Soc.*, 2010, **132**, 7005; (b) Q. K. Liu, J. P. Ma and Y. B. Dong, *Chem. Commun.*, 2011, **47**, 12343; (c) L. Duan, Z. H. Wu, J. P. Ma, X. W. Wu and Y. B. Dong, *Inorg. Chem.*, 2010, 49, 11164; (d) C. M. Liu, D. Q. Zhang, X. Hao and D. B. Zhu, *Eur. J. Inorg. Chem.*, 2012, 4210.

4 (a) C. M. Aikens, S. Z. Li and G. C. Schatz, *J. Phys. Chem. C*, 2008, **112**, 11272; (b) R. Satapathy, Y. H. Wu and H. C. Lin, *Org. Lett.*, 2012, **14**, 2564; (c) P. J. Stang, *J. Am. Chem. Soc.*, 2012, **134**, 11829; (d) C. B. Tian, H. B. Zhang, Y. Peng, Y. E. Xie, P. Lin, Z. H. Li and S. W. Du, *Eur. J. Inorg. Chem.* 2012, 4029.

5 (a) A. Yella, H. W. Lee, H. N. Tsao, C. Yi, A. K. Chandiran, M. K. Nazeeruddin, E. W. G. Diau, C. Y.Yeh, S. M. Zakeeruddin and M. Grätzel, *Science*, 2011, **334**, 629; (b) C. M. Lan, H. P. Wu, T. Y. Pan, C. W. Chang, W. S. Chao, C. T. Chen, C. L. Wang, C. Y. Lin and E. W. G. Diau, *Energy Environ. Sci.*, 2012, **5**, 6460; (c) M. Mojiri-Foroushani, H. Dehghani and N. Salehi-Vanani, *Electrochimica Acta*, 2013, **92**, 315.

6 (a) X. Wang, Y. L. Yang, P. Wang, L. Li, R. Q. Fan, W. W. Cao, B. Yang, H. Wang

and J. Y. Liu, *Dalton Trans*., 2012, **41**, 10619; (b) L. Y. Zhang, Y. L. Yang, R. Q. Fan, P. Wang and L. Li, *Dyes Pigm*., 2012, **92**, 1314.

7 (a) S. M. Li, X. J. Zheng, D. Q. Yuan, A. Ablet and L. P. Jin, *Inorg. Chem*., 2012, **51**, 1201; (b) K. K. Tanabe, C. A. Allen and S. M. Cohen, *Angew. Chem. Int. Ed*., 2010, **49**, 9730; (c) R. Feng, F. L. Jiang, L. Chen, C. F. Yan, M. Y. Wu and M. C. Hong, *Chem. Commun*., 2009, **45**, 5296; (d) H. Wang, D. Qi, Z. Xie, W. Cao, K. Wang, H. Shang and J. Jiang, *Chem. Commun*., 2013, **49**, 889.

8 (a) L. Sacconi, *Coord. Chem. Rev*., 1966, **1**, 126; (b) S. Yamada, *Coord. Chem. Rev*., 1966, **1**, 415; (c) C. Mehrotra, G. Srivastva and B. S. Saraswat, *Rev. Silicon, Germanium, Tin, Lead Compd*., 1982, **6**, 171; (d) M. Nath and S. Goyal, *Main Group Met. Chem*., 1995, **19**, 75.

9 H. L. Siddiqui, A. Iqbal, S. Ahmad and G. W. Weaver, *Molecules*, 2006, **11**, 206.

10 E. Hadjoudis and I. M. Mavridis, *Chem. Soc. Rev*., 2004, **33**, 579.

11 (a) M. Sliwa, S. Letard, I. Malfant, M. Nierlich, P. G. Lacroix, T. Asahi, H. Masuhara, P. Yu and K. Nakatani, *Chem. Mater.*, 2005, **17**, 4727; (b) M. Irie, *Chem. Rev*., 2000, **100**, 1683; (c) R. V. Andes and D. M. Manikowski, *Appl. Opt*., 1968, **7**, 1179.

12 (a) B. Machura, I. Nawrot and K. Michalik, *Polyhedron*, 2011, **30**, 2619; (b) X. M. Zhang, Z. M. Hao and H. S. Wu, *Inorg. Chem*., 2005, **44**, 7301; (c) Q. Ma, M. L. Zhu, C. X. Yuan, S. S. Feng, L. P. Lu and Q. M. Wang, *Cryst. Growth Des*., 2010, **10**, 1706; (d) M. Du, S. T. Chen and X. H. Bu, *Cryst. Growth Des.,* 2002, **2**, 625.

13 P. F. Yan, S. Chen, P. Chen, J. W. Zhang and G. M. Li, *CryEngComm*., 2011, **13**, 36.

14 J.G. Malecki, *Polyhedron*, 2010, **29**, 2489.

15 (a) M. K. Wang, N. Chamberland, L. Breau, J. E. Moser, R. Humphry-Baker, B. Marsan, S. M. Zakeeruddin and M. Grätzel, *Nat. Chem*., 2010, **2**, 385; (b) H. N. Tian, L. C. Sun, *J. Mater. Chem*., 2011, **21**, 10592; (c) L. Han, A. Islam, H. Chen, C. Malapaka, S. Zhang, X. Yang, M. Yanagida and B. Chiranjeevi, *Energy Environ. Sci*., 2012, **5**, 6057.

16 N. Gimeno and R. Vilar, *Coord. Chem. Rev.*, 2006, **250**, 3161.

17 A. Garoufis, S. Kasselouri, C. P. Raptopoulou and A. Terzis, *Polyhedron*, 1999, **18**, 585.

18 P. Baran, R. Boca, M. Breza, H. Elias, H. Fuess, V. Jorik, R. Klement and I. Svoboda, *Polyhedron*, 2002, **21**, 1561.

19 J. J. Lopex-Garriga, S. Hanton, G. T. Hanton, G. T. Babcock and J. F. Harrison, *J. Am. Chem. Soc.*, 1986, **108**, 7251.

20 X. M. Liu, H. Xia, W. Gao, Q. L. Wu. X. Fan, Y. Mu and C. S. Ma, *J. Mater. Chem*., 2012, **22**, 3485.

21 (a) C. J. Höller, P. R. Matthes, M. Adlung, C. Wickleder and K. Müller-Buschbaum, *Eur. J. Inorg. Chem*., 2012, 5479; (b) S. Gao, R. Q. Fan, L. S. Qiang, P. Wang, S. Chen, X. M. Wang and Y. L. Yang, *CrystEngComm*., 2014, **16**, 1113.

22 X. M. Liu, X. Y. Mu, H. Xia, L. Ye, W. Gao, H. Y. Wang, Y. Mu, *Eur. J. Inorg. Chem.*, 2006, 4317.

23 A. Bondi, *J. Phys. Chem*., 1964, **68**, 441.

24 A. W. Addison, T. N. Rao, J. Reedijk, J. van Rijn and G. C. Verschoor, *J. Chem. Soc. Dalton Trans*., 1984, 1349.

25 V. W.W. Yam, Y. L. Pui and K. K. Cheung, *New J. Chem.*, 1999, **23**, 1163.

26 (a) R. Q. Fan, L. Y. Wang, H. Chen, G. P. Zhou, Y. L. Yang, W. Hasi and W. W. Cao, *Polyhedron*, 2012, **33**, 90; (b) R. Q. Fan, Y. L. Yang, Y. B. Yin, W. Hasi and Y. Mu, *Inorg. Chem*., 2009, **48**, 6034.

27 X. M. Wang, R. Q. Fan, L. S. Qiang, W. Q. Li, P. Wang, H. J. Zhang and Y. L. Yang, *Chem. Commun*., 2014, **50**, 5023.

28 T. S. Basu Baul, S. Kundu, S. Mitra, H. Hopfl, E. R. T. Tiekink and A. Linden, *Dalton Trans*., 2013, **42**, 1905.

29 K. C. Stylianou, R. Heck, S. Y. Chong, J. Bacsa, J. T. A. Jones, Y. Z. Khimyak, D. Bradshaw and M. J. Rosseinsky, *J. Am. Chem. Soc*., 2010, **132**, 4119.

30 C. M. Liu, Z. Qi, C. G. Ma, P. Dorenbos, D. Hou, S. Zhang, X. J. Kuang, J. H. Zhang and H. Liang, *Chem. Mater*., Doi: 10.1021/cm501055k.

31 (a) C. X. Qin, Y. L. Huang, L. Shi, G. Q. Chen, X. B. Qiao and H. J. Seo, J. *Phys.*

D: Appl. Phys., 2009, **42**, 185105; (b) J. S. Kim, Y. H. Park, S. M. Kim, J. C. Choi and H. L. Park, *Solid State Commun*., 2005, **133**, 445; (c) D. Hsu and J. L. Skinner, *J. Chem*. *Phys*., 1984, **81**, 5471.

32 (a) X. X. Zhou, H. H. Cai, Y. Y. Ge, Z. Y. Zhou, Z. G. Gu, X. Gong, G. Zhao, Q. G. Zhang, R. H. Zeng and Y. P. Cai, *Cryst*. *Growth Des*., 2010, **10**, 4014; (b) F. Jin, H. Z. Wang, Y. Zhang, Y. Wang, J. Zhang, L. Kong, F. Y. Hao, J. X. Yang, J. Y. Wu, Y. P. Tian and H. P. Zhou, *CrystEngComm*, 2013, **15**, 3687.

33 K. D. Murugan and P. Natarajan, *Eur. Polym. J*., 2011, **47**, 1664.

34 N. Kundu, A. Audhya, S. M. T. Abtab, S. Ghosh, E. R. T. Tiekink and M. Chaudhury, *Cryst*. *Growth Des*., 2010, **10**, 1269.

35 C. M. Cardona, W. Li, A. E. Kaifer, D. Stockdale and G. C. Bazan, *Adv*. *Mater*., 2011, 23, 2367.

36 G. Boschloo, L. Häggman and A. Hagfeldt, *J*. *Phys*. *Chem*. *B*, 2006, **110**, 13144.

37 K. R. Justin Thomas, Y. C. Hsu, J. T. Lin, K. M. Lee, K. C. Ho, C. H. Lai, Y. M. Cheng and P. T. Chou, *Chem*. *Mater*., 2008, **20**, 1830.

38 (a) J. Bisquert, *J*. *Phys*. *Chem*. *B*, 2002, **106**, 325; (b) J. Bisquert, A. Zaban, M. Greenshtein and I. Mora-Sero, *J*. *Am*. *Chem*. *Soc*., 2004, **126**, 13550.

39 (a) J. Bisquert, *Phys. Chem. Chem. Phys.* 2003, **5**, 5360; (b) D. Kuang, S. Uchida, R. Humphry-Baker, S. M. Zakeeruddin and M. Grätzel, *Angew. Chem. Int. Ed.*, 2008, **47**, 1923; (c) N. Koide, A. Islam, Y. Chiba and L. Y. Han, *J. Photochem. Photobiol. A Chem.*, 2006, **182**, 296.

40 (a) C. P. Hsu, K. M. Lee, J. T. W. Huang, C. Y. Lin, C. H. Lee, L. P. Wang, S. Y. Tsai and K. C. Ho, *Electrochimica Acta.*, 2008, **53**, 7514; (b) K. E. Lee, M. A. Gomez, C. Charbonneau and G. P. Demopoulos, *Electrochimica Acta.*, 2012, **67**, 208; (c) C. Y. Hsu, W. T. Chen, Y. C. Chen, H. Y.Wei, Y. S. Yen, K. C. Huang, K. C. Ho, C. W. Chu and J. T. Lin, *Electrochimica Acta.*, 2012, **66**, 210.

41 S. Ito, P. Liska, P. Comte, R. Charvet, P. Pechy, U. Bach, L. Schmidt-Mende, S. M. Zakeeruddin, A. Kay, M. K. Nazeeruddin and M. Graetzel, *Chem*. *Commun*., 2005, **25**, 4351.

Table 1. Crystallographic and structural determination data for complexes **Zn1**–**Zn3**, **Cd1**–**Cd3** and **Hg1**–**Hg3**.

	Zn1	**Cd1**	**Hg1**	**Zn2**
CCDC No.	1025945	1025946	1025947	1205948
formula	$C_{19}H_{24}Cl_2N_2OZn$	$[C_{19}H_{24}Cl_2N_2OCd]_2$	$C_{19}H_{24}Cl_2N_2OHg$	$C_{14}H_{14}Cl_2N_2OZn$
Mr	432.67	959.42	567.89	362.56
crystal system	Monoclinic	Monoclinic	Monoclinic	Triclinic
space group	$P2_1/c$	$P2_1/c$	$P2_1/n$	$P\bar{1}$
a [Å]	10.050(5)	10.206(2)	9.3270(19)	8.0251(8)
b [Å]	17.306(5)	20.164(4)	16.828(3)	9.2087(9)
c [Å]	14.363(4)	21.555(4)	13.927(3)	10.4640(10)
α [˚]	90	90	90	95.054(8)
β [˚]	124.430(16)	94.96(3)	94.73(3)	93.455(8)
γ [˚]	90	90	90	92.379(8)
Volume [Å^3]	2060.5(13)	4419.3(15)	2178.5(8)	768.04(13)
Z	4	4	4	2
ρ_{calcd} [Mg m^{-3}]	1.395	1.442	1.732	1.568
μ, mm^{-1}	1.460	1.238	7.319	1.942
F(000)	896	1936	1096	368
θ limit [˚]	3.11˚ to 27.48˚	3.02˚ to 27.48˚	2.99˚ to 27.48˚	3.09˚ to 29.35˚
hkl index ranges	–13 ≤ h ≤ 13	–11 ≤ h ≤ 13	–12 ≤ h ≤ 12	–9 ≤ h ≤ 10
	–19 ≤ k ≤ 22	–26 ≤ k ≤ 26	–21 ≤ k ≤ 21	–12 ≤ k ≤ 10
	–18 ≤ l ≤ 18	–26 ≤ l ≤ 27	–18 ≤ l ≤ 16	–13 ≤ l ≤ 10
Data/restraints/parameters	4705 / 7 / 231	9952 / 0 / 451	4973 / 0 / 227	3495 / 0 / 181
GOF on F^2	1.034	0.994	0.827	0.951
R_1, wR_2[I>2σ(I)][a]	R_1 = 0.0405	R_1 = 0.0453	R_1 = 0.0319	R_1 = 0.0736
	wR_2 = 0.1005	wR_2 = 0.0949	wR_2 = 0.1034	wR_2 = 0.1606
R_1, wR_2[all data][a]	R_1 = 0.0537	R_1 = 0.0672	R_1 = 0.0447	R_1 = 0.1561
	wR_2 = 0.1078	wR_2 = 1011	wR_2 = 0.1163	wR_2 = 0.2146
Max. diff. peak/hole [e Å^{-3}]	0.675/–0.560	0.687/–0.551	0.999/–0.685	0.584/–0.398

Cd2	**Hg2**	**Zn3**	**Cd3**	**Hg3**
1025949	1025950	1026069	1025951	1025952
$C_{14}H_{14}Cl_2N_2OCd$	$C_{14}H_{14}Cl_2N_2OHg$	$C_{14}H_{14}Cl_2N_2O_2Zn$	$C_{14}H_{14}Cl_2N_2O_2Cd$	$C_{14}H_{14}Cl_2N_2O_2Hg$
409.58	497.76	378.56	425.57	513.76
Triclinic	Triclinic	Monoclinic	Monoclinic	Monoclinic
$P\bar{1}$	$P1$	$P2_1/c$	$P2_1/c$	$P2_1/c$
8.0765(5)	7.9723(5)	7.7220(15)	8.0890(16)	8.1151(4)
9.3574(5)	9.3550(5)	19.870(4)	26.743(5)	27.0756(10)
10.5442(5)	10.6022(10)	10.576(2)	7.8060(16)	7.9481(4)
94.409(4)	94.084(6)	90	90	90
93.636(4)	93.391(6)	91.50(3)	113.11(3)	114.015(6)
92.850(4)	93.839(5)	90	90	90
791.73(7)	785.32(10)	1622.2(5)	1553.1(5)	1595.20(13)
1	2	4	4	4
1.718	2.105	1.550	1.820	2.139
1.712	10.135	1.847	1.754	9.987
404	468	768	840	968

3.04˚ to 29.25˚	3.31˚ to 25.98˚	3.34˚ to 25.00˚	3.05˚ to 27.48˚	3.12˚ to 27.56˚
$-11 \le h \le 10$	$-9 \le h \le 9$	$-9 \le h \le 9$	$-9 \le h \le 10$	$-6 \le h \le 10$
$-12 \le k \le 11$	$-11 \le k \le 11$	$-23 \le k \le 23$	$-34 \le k \le 34$	$-35 \le k \le 15$
$-11 \le l \le 14$	$-13 \le l \le 10$	$-12 \le l \le 12$	$-10 \le l \le 10$	$-10 \le l \le 4$
3661 / 0 / 182	3063 / 0 / 182	2845 / 0 / 190	3549 / 0 / 190	3660 / 0 / 190
1.037	1.046	1.085	0.810	1.038
$R_1 = 0.0337$	$R_1 = 0.0530$	$R_1 = 0.0796$	$R_1 = 0.0553$	$R_1 = 0.0426$
$wR_2 = 0.0710$	$wR_2 = 0.1125$	$wR_2 = 0.1917$	$wR_2 = 0.1212$	$wR_2 = 0.0762$
$R_1 = 0.0431$	$R_1 = 0.0608$	$R_1 = 0.1056$	$R_1 = 0.0791$	$R_1 = 0.0648$
$wR_2 = 0.0784$	$wR_2 = 0.1221$	$wR_2 = 0.2072$	$wR_2 = 0.1419$	$wR_2 = 0.0857$
0.491/–0.752	2.807/–2.296	1.108/–0.714	1.243/–1.050	0.726/–1.315

[a] $R_1 = \sum||F_o| - |F_c||/\sum|F_o|$; $wR_2 = [\sum[w\,(F_o^2 - F_c^2)^2]/\sum[\,w\,(F_o^2)^2]]^{1/2}$.

Table 2. Photoluminescent data for ligands $\mathbf{L_1}$–$\mathbf{L_3}$ and complexes **Zn1**–**Zn3**, **Cd1**–**Cd3** and **Hg1**–**Hg3** at 298 K.

Complex	Absorption[a] (ε) (nm, $dm^3mol^{-1}cm^{-1}$)	Emission (λ_{max}, nm)	FWHM (nm)	Decay lifetime (τ, μs)	Quantum yields[a] (Φ)	Medium (298 K)	CIE (x, y)
$\mathbf{L_1}$	300 (4741)	400	62.0	7.92	0.023	CH_3CN	0.21 0.19
		500	95.3	10.80		solid	0.28 0.35
Zn1	316 (20184)	406	102.3	12.68	0.060	CH_3CN	0.17 0.10
		511	130.4	14.08		solid	0.27 0.35
Cd1	305 (13926)	408	86.5	10.79	0.033	CH_3CN	0.17 0.09
		509	160.9	13.19		solid	0.29 0.36
Hg1	303 (10219)	402	67.9	9.68	0.027	CH_3CN	0.21 0.11
		520	182.2	12.20		solid	0.29 0.43
$\mathbf{L_2}$	338 (6156)	411	65.3	6.05	0.054	CH_3CN	0.15 0.06
		508	85.5	11.74		solid	0.28 0.43
Zn2	366 (35603)	415	85.1	11.41	0.197	CH_3CN	0.17 0.11
		520	103.9	16.44		solid	0.31 0.52
Cd2	362 (21028)	427	79.3	13.36	0.070	CH_3CN	0.16 0.10
		510	90.2	16.98		solid	0.28 0.53
Hg2	352 (13964)	418	78.1	9.64	0.061	CH_3CN	0.18 0.11

		527	84.7	14.53		solid	0.31 0.48
L_3	353 (5237)	421	102.4	5.22	0.048	CH_3CN	0.23 0.21
		521	188.2	13.06		Solid	0.30 0.39
Zn3	385 (54004)	423	62.6	13.33	0.422	CH_3CN	0.17 0.09
		543	123.0	19.82		solid	0.38 0.53
Cd3	379 (27289)	450	176.6	12.36	0.156	CH_3CN	0.25 0.29
		528	89.6	15.37		solid	0.36 0.57
Hg3	362 (15059)	430	77.2	8.82	0.056	CH_3CN	0.18 0.14
		539	98.9	14.95		solid	0.37 0.54

[a] Recorded in acetonitrile at 298 K, concentration = 10^{-5} mol L^{-1}.

Table 3. Photoluminescent data for ligands $\mathbf{L_1}$–$\mathbf{L_3}$ and complexes **Zn1**–**Zn3**, **Cd1**–**Cd3** and **Hg1**–**Hg3** at 77 K.

Complex	Emission (λ_{max}, nm)	FWHM (nm)	Decay lifetime (τ, μs)	Medium (77 K)	CIE (x, y)
$\mathbf{L_1}$	484	84.4	6.14	CH_3CN	0.27 0.41
	486	197.5	6.33	solid	0.25 0.31
Zn1	494	136.0	7.62	CH_3CN	0.32 0.45
	499	131.0	11.36	solid	0.23 0.31
Cd1	489	105.0	6.53	CH_3CN	0.29 0.46
	488	138.7	10.74	solid	0.31 0.42
Hg1	489	66.1	6.39	CH_3CN	0.28 0.46
	490	68.9	6.47	solid	0.28 0.47
$\mathbf{L_2}$	505	93.2	5.90	CH_3CN	0.28 0.45
	510	131.5	6.31	solid	0.28 0.40
Zn2	531	96.8	8.44	CH_3CN	0.38 0.56
	520	84.5	10.74	solid	0.33 0.59
Cd2	510	85.0	7.22	CH_3CN	0.31 0.57
	512	76.7	8.96	solid	0.30 0.58
Hg2	529	106.9	6.65	CH_3CN	0.36 0.53
	510	91.5	6.93	solid	0.33 0.44
$\mathbf{L_3}$	527	111.9	4.46	CH_3CN	0.36 0.53
	530	205.4	5.90	solid	0.32 0.42
Zn3	591	140.1	8.83	CH_3CN	0.47 0.51
	557	88.4	14.27	solid	0.41 0.54
Cd3	576	148.8	8.63	CH_3CN	0.42 0.48
	545	85.7	10.75	solid	0.39 0.58
Hg3	545	88.4	7.11	CH_3CN	0.40 0.57
	532	99.9	9.45	solid	0.34 0.46

Table 4. Experimental data for spectral and electrochemical properties of the synthesized complexes **Zn1**–**Zn3**.

Dyes	λ_{abs}(nm)[a]	$\varepsilon(M^{-1}cm^{-1})$[a]	λ_{em}(nm)[a,b]	$E_{0\text{-}0}$(eV)[c]	E_{HOMO}(eV)[d]	E_{LUMO}(eV)[d]
Zn1	342	24975	472	3.04	-5.18	-2.14
Zn2	361	29727	488	3.01	-4.86	-1.85
Zn3	378	33460	502	2.94	-5.02	-2.08

[a] Absorption and emission spectra were recorded in ethanol solution (3×10^{-4} M) at room temperature.

[b] Complexes were excited at their absorption maximum value

[c] Optical band gap calculated from intersection between the absorption and emission spectra.

[d] The values of E_{HOMO} and E_{LUMO} were calculated with the following formula:

$$HOMO\ (eV) = -e(E^{ox}_{onset}V + 4.4V); \quad LUMO\ (eV) = E_{HOMO} + E_{0\text{-}0}$$

where $E_{0\text{-}0}$ is the intersection of absorption and emission of the complexes.

Table 5. *J-V* performance of DSSCs based on different photoelectrodes.

Photoelectrode	J_{sc}/mA/cm^2	V_{oc}/V	*FF*	η/%
N719/TiO_2	11.19	0.70	0.65	5.11
Zn1/N719/TiO_2	13.88	0.69	0.58	5.63
Zn2/N719/TiO_2	14.81	0.71	0.60	6.35
Zn3/N719/TiO_2	16.59	0.72	0.58	6.94

Table of Content

Synthesis and Characterization of Substituted Schiff-base Ligands and Their d^{10} Metal Complexes: Structure-induced Luminescence Tuning Behaviors and Applications in Co-sensitized Solar Cells

Yu-Wei Dong,[a] Rui-Qing Fan,*[a] Ping Wang,[a] Li-Guo Wei,[a] Xin-Ming Wang,[a] Hui-Jie Zhang,[a] Song Gao,[a] Yu-Lin Yang*[a] and Yu-Lei Wang[b]

[a]*Department of Chemistry, Harbin Institute of Technology, Harbin 150001, P. R. of China*

[b]*National Key Laboratory of Science and Technology on Tunable Laser, Harbin Institute of Technology, Harbin 150080, P. R. of China*

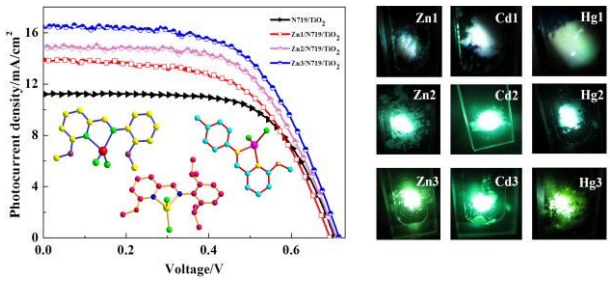

The structure-induced luminescence tuning behaviors of schiff-base ligand based d^{10} metal complexes and their applications in co-sensitized solar.